A Decomposition Technique of Generalized Degrees of Freedom for Mixed-mode Crack Problems

Huo Fan[1,2,3,4] **Hong Zheng**[5] **Chunguang Li**[5] **Siming He**[1,2,3,*,†]

1. Key Laboratory of Mountain Hazards and Surface Process, Chinese Academy of Science, Chengdu 610041, China;
2. Institute of Mountain Hazards and Environment, Chinese Academy of Sciences, Chengdu 610041, China;
3. Center for Excellence in Tibetan Plateau Earth Sciences, Chinese Academy of Sciences, Beijing 100101,China;
4. University of Chinese Academy of Sciences, Beijing 100049, China;
5. State Key Laboratory of Geomechanics and Geotechnical Engineering, Chinese Academy of Sciences, Wuhan 430071, China.

SUMMARY

The numerical manifold method (NMM) builds up a unified framework that is used to describe continuous and discontinuous problems; it is an attractive method for simulating a cracking phenomenon. Taking into account the differences between the generalized degrees of freedom of the physical patch and nodal displacement of the element in the NMM, a decomposition technique of generalized degrees of freedom is deduced for mixed mode crack problems. An analytic expression of the energy release rate, which is caused by a virtual crack extension technique (VCET), is proposed. The necessity of using a symmetric mesh is demonstrated in detail by analysing an additional error that had previously been overlooked. Because of this necessity, the local mathematical cover refinement is further applied. Finally, four comparison tests are given to illustrate the validity and practicality of the proposed method. The abovementioned aspects are all implemented in the high-order NMM, so this study can be regarded as the development of the VCET and can also be seen as a prelude to an h-version high-order NMM.

KEY WORDS: Numerical manifold method; Virtual crack extension; Energy release rate; Decomposition of generalized degrees of freedom; Mathematical cover refinement

***Correspondence to: Siming. Key Laboratory of Mountain Hazards and Surface Process, Chinese Academy of Science, Chengdu 610041, China.**

†E-mail address: hsm_imde@163.com

This article has been accepted for publication and undergone full peer review but has not been through the copyediting, typesetting, pagination and proofreading process which may lead to differences between this version and the Version of Record. Please cite this article as doi: 10.1002/nme.5533

1. INTRODUCTION

To date, various technologies and strategies of extracting stress intensity factors (SIFs, particularly the coefficient of a singularity) [1] or of calculating strain-energy release rates have been put forward in computational linear elastic fracture mechanics. First, Griffith's energy [2] can be used. The path-independent line J-integral was suggested by [3]. The displacement extrapolation technique based on SIF curves has also been employed [4]. A quarter-point elements technique was originated [5–7]. By following the concept of the crack closure integral [8], the virtual crack-closure technique was presented by [9, 10]. The field decomposition was presented [11] for mixed mode crack. The equivalent domain integral was derived [12, 13]. An interaction integral technique involving actual and auxiliary fields can be found in [14, 15]. The discontinuous enrichment function [16] can also reflect the singularity of the crack tip fields. Some similar techniques were then used in the extended finite element method (XFEM) [17, 18]. By making use of the properties of XFEM, an analytical approach to extract the strain-energy release rates was provided by [19]. Under the context of XFEM, a direct analytical method to extract the mixed-mode strain-energy release rates from Irwin's integral was given by [20], and then this method was extended to high-order XFEM [21,22].

Alternatively, the stiffness derivative technique (SDT) and virtual crack extension techniques (VCET) were proposed, respectively [23, 24]. Whereafter, the VCET was applied to determine the SIFs of mode-I and mode-II by carrying out virtual crack extension along both the parallel and perpendicular directions to crack surface [25]. A combination of the VCET and field decomposition technique was initially implemented to extract mixed-mode SIFs by carrying out virtual crack extension in only the parallel direction to crack surface [26]. A double VCET for crack growth stability assessment was described by [27]. Based on an energy principle and the VCET, an approach that does not require the use of symmetric crack-tip mesh nor crack-tip singular elements was developed [28]. The VCET was used for simulation of the fatigue crack propagation by [29, 30]. In order to avoid using finite difference approximation, which can lead to calculation error, an analytical expression for the energy release rate was derived [31]; another explicit expression for energy changes due to VCET was formulated based on a variation of isoparametric element mappings [32]. A new direct-integration technique for the VCET using variational theory was presented in [33]. A blend of the VCET and field decomposition technique was implemented to decompose there-dimensional mixed-mode energy release rates [34].

The concept of shape design sensitivity analysis [35] was applied to calculate the strain-energy release rate [36]. And then, the equivalent domain integral [37] and the interaction integral [38] were used for the sensitivity analysis of cracked bodies. From the view of the shape design sensitivity analysis, where the crack length is regarded as a single design variable, an analytical method to calculate the stiffness derivative was put forward and the equivalence of the stiffness derivative and the equivalent domain integral was proved in detail by [39], and a new error estimator was suggested by [40, 41] for the mixed-mode energy release rates. Consider that the task of a shape design sensitivity analysis or shape optimization is to obtain the variation of the structural response along with the change in the design parameters, therefore, a generalized shape optimization tool proposed by [42, 43] may can be applied to estimate strain-energy release rates or SIFs. Besides, the continuum shape sensitivity methods to calculate mixed-mode SIFs for isotropic and orthotropic functionally graded material were presented by [44, 45], respectively. Recently, this tool based on XFEM and level set [46] was employed in the shape optimization of bi-material structures [47] and the damage process sensitivity analysis [48].

On the other hand, the NMM with its dual cover system, i.e. the mathematical cover and the physical cover, was initially developed in [49]. It is worth mentioning that a simplex integration method for NMM, finite element method (FEM), discontinuous deformation analysis, and analytical analysis was proposed in [50]. From a more general perspective, the NMM also falls into methods based on the partition of unity (PU) [51]. Therefore, by increasing the order of PU function, it is easier to raise the order of approximate solutions. Formulations of the high-order approximations were derived in detail in [52]. Correspondingly, the simplex integration strategy and programming of high-order NMMs were studied in [53–55]. Like other PU-based methods, the linear dependence problem [56] exists in high-order NMM and leads directly to the singularity in a global stiffness matrix. An algorithm for predicting the rank deficiency of the global stiffness matrix was proposed in [57], and this algorithm was extended in [58]. Recently, a new procedure to eliminate the linear dependence was created by [59]. It is worth mentioning that the S(strain)-R(rotation)-based NMM proposed by [60] enhances the ability of dealing with large deformation and large rotation effectively. Complex crack problems were modelled using the NMM in [61]. The cracking behaviour of rock mass containing inclusions was modelled using the NMM by [62]. Extraction of stress intensity factors on honeycomb elements by the NMM was completed in [63]. Not long ago, some new strategies for solving the issues in the NMM for simulation of crack propagation were proposed in [64].

In 2002, the federation pattern of the SDT or VCET and the displacement field decomposition techniques (DFDT) was introduced into the NMM in [65]. This usage pattern was initially given in [28] for the FEM. In [65], the finite difference scheme was used to approximate the stiffness derivative, and the nodal displacement vector still appeared explicitly in the expression of the potential energy of a system. Strictly speaking, for cover-based methods such as the NMM, the generalized degrees of freedom vector should be present in the expression of the potential energy rather than the nodal displacement vector. Moreover, before [28], some geometry symmetric elements with respect to the local x-axis of the local crack-tip coordinate system were almost always adopted in the abovementioned usage pattern. However, this symmetrical configuration was removed by [28] and [65]. Thus, an additional error, which had been overlooked, was introduced in spite of the fact that the error can be suppressed by mesh refinement.

In this study, a decomposition technique aiming at the generalized degrees of freedom is proposed. Furthermore, using the VCET, a new analytic expression of stiffness derivative is derived based on the simplex integration method [50]. Moreover, the sources of the additional error, which is named as the mixed terms error in this work, are analysed in detail. In addition, the local mathematical cover refinement (LMCR), which involves the refinement of the domain adjacent to the crack-tip, is further applied in the high-order NMM advised in [66]. In fact, this LMCR has been used in [65], [67], and [68] with the first-order NMM. Therefore, this study can be regarded as the development of the VCET and SDT and can also be seen as a prelude to an h-version high-order NMM.

2. BRIEF DESCRIPTION OF NMM

The NMM [49] is composed of four related parts [69]: the cover systems, the partition of unity, the NMM space, and the variational formulation fitted to the method. One can refer to the references [49], [64], [69], and [70] for more details about the orthodox statements of the NMM.

The problem domain, Ω, as shown in figure 1, consists of a black solid boundary and black dotted line representing a crack surface. The mathematical cover (MC) is a collection of simply connected geometries, i.e. the red polygons and circles. These simply connected geometries can, in principle, be of arbitrary shape. Any simply connected geometry is called a mathematical patch (MP). Different MPs can overlap partially, but all the MPs must cover the Ω totally. The configuration of the MC, including the size and shape of the geometries, determines the precision of the solution. By cutting all of the MPs, one after another, with the Ω's components, including the boundary, material interface, and the crack, the physical patches (PPs) are created. All of the PPs then form the physical cover (PC), in other words, the PC is the collection of all PPs. Each PP might be divided into several domains by the neighbouring PPs, and a manifold element (ME) is a common part of a group of PPs.

Next, the six-node triangular mesh is taken as an example (figure 2) to illustrate the forming process of the ME in more detail because it is closely related to the assembly of the global stiffness matrix.

Assume that the triangle ΔABC is the problem domain, Ω. The thick lines AB, BC, and CA are the boundaries of Ω, whereas the thick dashed line DF is either a weak or strong discontinuity interface. Boundaries and interfaces are referred to as the components of Ω. Considering the triangle $\Delta 142536$, under the finite element mesh cover, all the triangles sharing an common node, which is referred to as a "star" in NMM, constitute an mathematical patch MP (it is a quadrangle or hexagon in this study). Let us see node 1, the corresponding MP is MP_1 (a hexagon), where the subscript "1" stands for the number of node 1; in the same way, for the rest nodes from nodes 2 to 6, the MPs are MP_2 (a hexagon), MP_3 (a quadrangle), MP_4 (a quadrangle), MP_5 (a quadrangle), and MP_6 (a quadrangle), respectively, as shown in figure 2. The physical patches are formed by slicing the mathematical patches with the components of Ω. For instance (see figure 3), firstly, let us focus on MP_1 (a red hexagon) and the problem domain Ω; then slice MP_1 using boundary lines AB, BC, CA, and interface line DF so that we can obtain points B', C', and F'; next generate physical patches $PP_{1\text{-}1}$ and $PP_{1\text{-}2}$. Therefore, we can say that physical patches $PP_{1\text{-}1}$ and $PP_{1\text{-}2}$ all stem from MP_1.

In the similar fashion, we can obtain PP_2, PP_{3-1}, PP_{3-2}, PP_{4-1}, PP_{4-2}, PP_{5-1}, PP_{5-2}, PP_{6-1}, and PP_{6-2}, as shown in figure 4. Then, the element ME is the overlap of PP_{1-2}, PP_2, PP_{3-2}, PP_{4-2}, PP_{5-2}, and PP_{6-2}, implying that every ME is affected by six physical patches in the used high-order NMM.

In this paper, the phenomenon where one mathematical patch is subdivided into several physical patches is referred to as the "MP split" or "star split", such as mathematical patch MP_1 is split into two physical patches PP_{1-1} and PP_{1-2}.

On the other hand, the shape function of the six-node triangle is chosen as the partition of unity, as shown in figure 5. The area coordinates of any point (x, y) in element ME is

$$L_k = \frac{a_k + b_k x + c_k y}{2\Delta}, \quad k = 1,2,3 \tag{1}$$

where

$$\Delta = \frac{1}{2} \det \begin{bmatrix} 1 & s_1 & t_1 \\ 1 & s_2 & t_2 \\ 1 & s_3 & t_3 \end{bmatrix} \tag{2}$$

and

$$a_1 = s_2 t_3 - s_3 t_2, \quad b_1 = t_2 - t_3, \quad c_1 = s_3 - s_2 \tag{3}$$

with cyclic rotation of indices 1, 2, and 3. (s_1, t_1), (s_2, t_2) and (s_3, t_3) are three "stars" of the triangular mesh covering the element ME.

For the three-node triangle, the partition of unity can be chosen as

$$\varphi_1 = L_1, \quad \varphi_2 = L_2, \quad \varphi_3 = L_3 \tag{4}$$

whereas for the six-node triangle, the partition of unity should be

Corner nodes:

$$\varphi_k = (2L_k - 1)L_k, \quad k = 1,2,3 \tag{5}$$

Mid-side nodes:

$$\varphi_4 = 4L_1L_2, \quad \varphi_5 = 4L_2L_3, \quad \varphi_6 = 4L_3L_1 \tag{6}$$

and $\varphi_i, i = 1,2,...,6$ can be written as

$$\begin{pmatrix} \varphi_1 \\ \varphi_2 \\ \varphi_3 \\ \varphi_4 \\ \varphi_5 \\ \varphi_6 \end{pmatrix} = \begin{pmatrix} f_{11} & f_{12} & f_{13} & f_{14} & f_{15} & f_{16} \\ f_{21} & f_{22} & f_{23} & f_{24} & f_{25} & f_{26} \\ f_{31} & f_{32} & f_{33} & f_{34} & f_{35} & f_{36} \\ f_{41} & f_{42} & f_{43} & f_{44} & f_{45} & f_{46} \\ f_{51} & f_{52} & f_{53} & f_{54} & f_{55} & f_{56} \\ f_{61} & f_{62} & f_{63} & f_{64} & f_{65} & f_{66} \end{pmatrix} \begin{pmatrix} 1 \\ x \\ y \\ x^2 \\ xy \\ y^2 \end{pmatrix} \tag{7}$$

where $f_{ij}, i, j = 1,2,...,6$ should be interpreted as some constants with respect to $s_i, t_i (i, j = 1,2,3)$. Their expressions can be found in [71]. Moreover, in this study, we take constants to be local approximations of PPs.

3. FORMULA FOR THE STIFFNESS DERIVATIVE

In this study, the local approximation of each PP is a constant and the displacement functions $u(x, y)$ and $v(x, y)$ of any point (x, y) in a ME can be written as [49]

$$\begin{Bmatrix} u(x,y) \\ v(x,y) \end{Bmatrix} = \sum_{i=1}^{6} \begin{bmatrix} \varphi_i(x,y) & 0 \\ 0 & \varphi_i(x,y) \end{bmatrix} \begin{Bmatrix} d_{2i-1} \\ d_{2i} \end{Bmatrix} \tag{8}$$

where $(d_1, d_2, d_3, d_4, d_5, d_6, d_7, d_8, d_9, d_{10}, d_{11}, d_{12})^{\mathrm{T}}$ is the generalized degrees of freedom vector of those patches sharing the same element.

Considering the global coordinate system, in the NMM framework, the total potential energy Π of a system can be written as

$$\left(\Pi = \frac{1}{2}\mathbf{D}^{\mathrm{T}}\mathbf{K}\mathbf{D} - \mathbf{D}^{\mathrm{T}}\mathbf{f} \right)_{global} \tag{9}$$

where $\mathbf{D}$ is the generalized degrees of freedom vector; $\mathbf{K}$ is the stiffness matrix; $\mathbf{f}$ is the equivalent force vector. Superscript T denotes transpose, and $(\cdot)_{global}$ is the representation in the global coordinate system.

As shown by Parks [23] and Hellen [24], the energy release rate G of the system for the unit crack extension can be calculated by differentiating the total potential energy with respect to the crack length

$$\left(G = -\frac{\partial \Pi}{b\partial l} = -\frac{\partial \mathbf{D}^{\mathrm{T}}}{b\partial l}(\mathbf{K}\mathbf{D} - \mathbf{f}) - \frac{1}{2}\mathbf{D}^{\mathrm{T}}\frac{\partial \mathbf{K}}{b\partial l}\mathbf{D} + \mathbf{D}^{\mathrm{T}}\frac{\partial \mathbf{f}}{b\partial l} \right)_{global} \tag{10}$$

where l is initial crack length and b is thickness, respectively. The term of $\partial \mathbf{K} / \partial l$ the so-called stiffness derivative. Under the context of the shape design sensitivity analysis, l can be seen as a design variable [39].The expression $\mathbf{K}\mathbf{D} - \mathbf{f}$ represents the system of equations and must therefore vanish. If we assume that the equivalent force vector $\mathbf{f}$ does not change with the crack length, Eq. (10) becomes

$$\left(G = -\frac{\partial \Pi}{b \partial l} = -\frac{1}{2} \mathbf{D}^{\mathrm{T}} \frac{\partial \mathbf{K}}{b \partial l} \mathbf{D} \right)_{global} \tag{11}$$

In [65], which is about the NMM, by using the difference approximation, the energy release rate G can be written as

$$\left(G = -\frac{1}{2} \mathbf{U}^{\mathrm{T}} \frac{\partial \mathbf{K}}{b \partial l} \mathbf{U} \approx -\frac{1}{2} \mathbf{U}^{\mathrm{T}} \frac{\mathbf{K}(l+\Delta l) - \mathbf{K}(l)}{b \Delta l} \mathbf{U} = -\frac{1}{2} \mathbf{U}^{\mathrm{T}} \frac{\Delta \mathbf{K}}{b \Delta l} \mathbf{U} \right)_{global} \tag{12}$$

where $\mathbf{U}$ is the nodal displacement vector. However, in the framework of the NMM, it should be pointed out that the above equation is valid only if one manifold element coincides exactly with the triangular mesh covering it. The above expression generally does not hold especially near the crack surfaces unless the MC matches the PC.

For example, figure 6(a) and (b) are the configurations of the pre-deformation and post-deformation, respectively. The bold black dotted line represents the crack surfaces. Here, we only pay attention to the six hatched elements, i.e., ME_1, ME_2, ME_3, ME_4, ME_5, and ME_6. The pulling force $\mathbf{F}$ is imposed on the configuration. Before deformation, several MPs covering these elements overlap each other; thus, only three triangular meshes are visible, i.e. the three purple triangles shown in figure 6(a). After deformation, the triangular meshes near the crack surfaces are all clearly visible, i.e. the three red triangles and three blue triangles, as shown in figure 6(b). In the case of figure 6, Eq. (12) obviously does not hold.

In this study, instead of the difference quotient $\Delta \mathbf{K} / \Delta l$, we implement a new computational formula for partial derivative of the element stiffness matrix based on the simplex integration proposed by Shi [49] with assistance from VCET. Figure 7 shows the simplest way of performing a virtual crack extension in which the crack-tip point is shifted in the crack direction by a small distance Δl. In this way, only the crack-tip elements contribute to the matrix $\partial \mathbf{K} / \partial l$, and the term $\partial \mathbf{f} / \partial l$ is null except when external forces are applied to the crack-tip elements. In addition, l is the initial length of crack line segment AB, whereas α is the inclined angle between crack line segment AB and the positive direction of the x-axis.

For any point $\mathrm{P}(x,y)$ on the line AB, its coordinate can be expressed as

$$\begin{pmatrix} x = x_{\mathrm{A}} + l \cos \alpha \\ y = y_{\mathrm{A}} + l \sin \alpha \end{pmatrix}_{global} \tag{13}$$

where $(x_{\mathrm{A}}, y_{\mathrm{A}})$ is the coordinate of point A. From Eq. (13), we can obtain

$$\begin{pmatrix} \frac{\mathrm{d}x}{\mathrm{d}l} = \cos\alpha \\ \frac{\mathrm{d}y}{\mathrm{d}l} = \sin\alpha \end{pmatrix}_{global} \tag{14}$$

After a continuum mechanics analogy, Eq. (14) can be named velocity field [39], which is of paramount importance in each shape design sensitivity analysis. As we know, the element stiffness matrix is

$$\left(\mathbf{k}(x,y) = \iint \mathbf{B}^{\mathrm{T}}(x,y)\mathbf{E}\mathbf{B}(x,y)\mathrm{d}A\right)_{global} \tag{15}$$

where $\mathbf{k}(x,y)$ is a quadratic functions with respect to x,y and point (x,y) is an arbitrary point in the triangular element, e.g. $\Delta 123$, which is the domain of integration. $\mathbf{E}$ is the elastic constitutive matrix and the strain-nodal displacement matrix $\mathbf{B}$ can be written as

$$\left(\mathbf{B} = \begin{bmatrix} \varphi_{i,x} & 0 \\ 0 & \varphi_{i,y} \\ \varphi_{i,y} & \varphi_{i,x} \end{bmatrix}\right)_{global} \quad ,i = 1,2,\ldots,6 \tag{16}$$

By using the simplex integration proposed by Shi [50], $\mathbf{k}$ can be expressed as a multivariate quadratic function, i.e. $\mathbf{k}(x_1, y_1, x_2, y_2, x_3, y_3, s_1, t_1, s_2, t_2, s_3, t_3)$. If the crack-tip is at point (x_1, y_1), and "star" (s_1, t_1) coincide with point (x_1, y_1), we can obtain

$$\left(\frac{\partial \mathbf{k}}{\partial l} = \frac{\partial \mathbf{k}}{\partial x_1}\frac{\mathrm{d}x_1}{\mathrm{d}l} + \frac{\partial \mathbf{k}}{\partial y_1}\frac{\mathrm{d}y_1}{\mathrm{d}l} + \frac{\partial \mathbf{k}}{\partial s_1}\frac{\mathrm{d}s_1}{\mathrm{d}l} + \frac{\partial \mathbf{k}}{\partial t_1}\frac{\mathrm{d}t_1}{\mathrm{d}l} = \cos\alpha\left(\frac{\partial \mathbf{k}}{\partial x_1} + \frac{\partial \mathbf{k}}{\partial s_1}\right) + \sin\alpha\left(\frac{\partial \mathbf{k}}{\partial y_1} + \frac{\partial \mathbf{k}}{\partial t_1}\right)\right)_{global} \tag{17}$$

Assume that the element nodes and the "stars" are all numbered randomly in a counterclockwise direction, so that there are the following nine cases:

$$\text{Crack-tip} \;—\; \text{point}(x_i, y_i) \;—\; \text{"star"}(s_j, t_j), \quad i, j = 1,2,3 \tag{18}$$

where "—" denotes that they are concurrent. For each case, one can obtain an expression similar to Eq. (17).

For any point, on the other hand, there is the following transformation

$$(x,y)^{\mathrm{T}}_{local} = \begin{pmatrix} \cos a & \sin a \\ -\sin a & \cos a \end{pmatrix} [(x,y)^{\mathrm{T}}_{global} - (x,y)^{\mathrm{T}}_{tip}] \tag{19}$$

where $(x,y)_{local}$ and $(x,y)_{global}$ are the local crack-tip coordinate and the global coordinate of any point, respectively. $(x,y)_{tip}$ is the global coordinate of the crack-tip point. Because the determinant of the Jacobian matrix used for coordinate transformation is unit, the modality of $(\partial \mathbf{k} / \partial l)_{local}$ in the local crack-tip coordinate system ($\alpha = 0$) is the same as one of $(\partial \mathbf{k} / \partial l)_{global}$ in the global coordinate system. Hence, Eq. (17) becomes

$$\left(\frac{\partial \mathbf{k}}{\partial l}\right)_{local} = \left(\frac{\partial \mathbf{k}}{\partial x_1} + \frac{\partial \mathbf{k}}{\partial s_1}\right)_{local} \tag{20}$$

where $(\cdot)_{local}$ is the representation in the local crack-tip coordinate system. Because the analytical expressions of $\mathbf{k}$ can be obtained through the simplex integration [50], Eq. (20) is then easy to calculate.

4. DECOMPOSITION TECHNIQUE OF GENERALIZED DEGREE OF FREEDOM

For FEM, in the local crack-tip coordinate system, Ishikawa et al. [11] pointed out that for a mixed mode crack, as shown in figure 8,

the mode-I and mode-II decomposed displacement components at arbitrary point A can be expressed as follows:

$$\begin{pmatrix} u_{I\mathrm{A}} = \frac{1}{2}(u_\mathrm{A} + u_\mathrm{B}), & u_{II\mathrm{A}} = \frac{1}{2}(u_\mathrm{A} - u_\mathrm{B}) \\ v_{I\mathrm{A}} = \frac{1}{2}(v_\mathrm{A} - v_\mathrm{B}), & v_{II\mathrm{A}} = \frac{1}{2}(v_\mathrm{A} + v_\mathrm{B}) \end{pmatrix}_{local} \tag{21}$$

where $(u_{I\mathrm{A}}, v_{I\mathrm{A}})$ and $(u_{II\mathrm{A}}, v_{II\mathrm{A}})$ are the Mode-I and Mode-II decomposed displacement with respect to point A, respectively. $(u_\mathrm{A}, v_\mathrm{A})$ is the displacement of point A, and $(u_\mathrm{B}, v_\mathrm{B})$ is the displacement of point B, which is the mirror image of point A.

Next, the decomposition technique of generalized degree of freedom for mixed-mode crack problems will be deduced based on Eq. (21), as shown in figure 9. Assume that the equilibrium equation of the system is established in the local crack-tip coordinate system, and then solve the equation to obtain the generalized degree of freedom vector with respect to the local crack-tip coordinate system.

For any crack-tip element and it's six "stars", i.e. element $\mathrm{ME_A}$ (here subscript "A" means that the element contains point A) and "stars" 1,2,3,4,5 or 6, one can construct the mirror element and mirror "stars", i.e. element $\mathrm{ME_B}$ (here subscript "B" means that the element contains point B) and "stars" 1*,2*,3*,4*,5* or 6*. For the arbitrary nodal point A of the crack-tip element, one can obtain

$$\left(\begin{Bmatrix} u_\mathrm{A} \\ v_\mathrm{A} \end{Bmatrix} = \sum_{i=1}^{6} \begin{bmatrix} \varphi_{i\mathrm{A}}(x,y) & 0 \\ 0 & \varphi_{i\mathrm{A}}(x,y) \end{bmatrix} \begin{Bmatrix} d_{2i-1} \\ d_{2i} \end{Bmatrix}_\mathrm{A} = \boldsymbol{\varphi}_\mathrm{A} \{d\}_\mathrm{A} \right)_{local} \tag{22}$$

where

$$\left(\boldsymbol{\varphi}_\mathrm{A} = \begin{bmatrix} \varphi_{1\mathrm{A}} & 0 & \varphi_{2\mathrm{A}} & 0 & \varphi_{3\mathrm{A}} & 0 & \varphi_{4\mathrm{A}} & 0 & \varphi_{5\mathrm{A}} & 0 & \varphi_{6\mathrm{A}} & 0 \\ 0 & \varphi_{1\mathrm{A}} & 0 & \varphi_{2\mathrm{A}} & 0 & \varphi_{3\mathrm{A}} & 0 & \varphi_{4\mathrm{A}} & 0 & \varphi_{5\mathrm{A}} & 0 & \varphi_{6\mathrm{A}} \end{bmatrix}\right)_{local} \tag{23}$$

One can refer to Eq. (7). And $\{d\}_\mathrm{A}$ is the solution vector corresponding to the element containing the point A. However, for the mirror image point B, because "stars" 1*,2*,3*,4*,5* and 6* are arranged in clockwise direction, we should rearrange them in the counterclockwise direction and redefine some variables, as shown below:

$$\left(\Delta_{\mathrm{B}} = \frac{1}{2}\det\begin{bmatrix} 1 & s_2^* & t_2^* \\ 1 & s_1^* & t_1^* \\ 1 & s_3^* & t_3^* \end{bmatrix}\right)_{local} \tag{24}$$

$$\left(a_{1\mathrm{B}} = s_3^* t_2^* - s_2^* t_3^*,\ b_{1\mathrm{B}} = t_3^* - t_2^*,\ c_{1\mathrm{B}} = s_2^* - s_3^*\right)_{local} \tag{25}$$

In the local crack-tip coordinate system, it is exits that

$$\left(\begin{Bmatrix} x_{\mathrm{B}} \\ y_{\mathrm{B}} \end{Bmatrix} = \begin{Bmatrix} x_{\mathrm{A}} \\ -y_{\mathrm{A}} \end{Bmatrix}\right)_{local},\ \left(\begin{Bmatrix} s_i \\ t_i \end{Bmatrix} = \begin{Bmatrix} s_i^* \\ -t_i^* \end{Bmatrix}\right)_{local},\ i = 1,2,\ldots,6 \tag{26}$$

where $(s_1^*, t_1^*), (s_2^*, t_2^*)$ and (s_3^*, t_3^*) are the coordinates of "stars" 1*, 2* and 3* respectively. Thus, we have

$$\left(\Delta_{\mathrm{B}} = \Delta_{\mathrm{A}}, a_{i\mathrm{B}} = a_{i\mathrm{A}},\ b_{i\mathrm{B}} = b_{i\mathrm{A}},\ c_{i\mathrm{B}} = -c_{i\mathrm{A}}\right)_{local},\quad i = 1,2,3 \tag{27}$$

Further, for the mirror image point B, one can obtain

$$\left(\begin{Bmatrix} u_{\mathrm{B}} \\ v_{\mathrm{B}} \end{Bmatrix} = \sum_{i=1}^{6} \begin{bmatrix} \varphi_{i\mathrm{B}}(x,y) & 0 \\ 0 & \varphi_{i\mathrm{B}}(x,y) \end{bmatrix} \begin{Bmatrix} d_{2i-1} \\ d_{2i} \end{Bmatrix}_{\mathrm{B}} = \boldsymbol{\varphi}_{\mathrm{B}} \{d\}_{\mathrm{B}}\right)_{local} \tag{28}$$

where

$$\left(\boldsymbol{\varphi}_{\mathrm{B}} = \begin{bmatrix} \varphi_{1\mathrm{B}} & 0 & \varphi_{2\mathrm{B}} & 0 & \varphi_{3\mathrm{B}} & 0 & \varphi_{4\mathrm{B}} & 0 & \varphi_{5\mathrm{B}} & 0 & \varphi_{6\mathrm{B}} & 0 \\ 0 & \varphi_{1\mathrm{B}} & 0 & \varphi_{2\mathrm{B}} & 0 & \varphi_{3\mathrm{B}} & 0 & \varphi_{4\mathrm{B}} & 0 & \varphi_{5\mathrm{B}} & 0 & \varphi_{6\mathrm{B}} \end{bmatrix}\right)_{local} \tag{29}$$

One can also refer to Eq. (7). And $\{d\}_{\mathrm{B}}$ is the solution vector corresponding to the element containing the point B. Using Eqs. (26) and (27), the following relationship can be verified easily

$$\left(\boldsymbol{\varphi}_{\mathrm{A}} = \boldsymbol{\varphi}_{\mathrm{B}}\right)_{local} \tag{30}$$

Now, due to Eq. (21), we have

$$\left(\begin{Bmatrix} u_{I\mathrm{A}} \\ v_{I\mathrm{A}} \end{Bmatrix} = \boldsymbol{\varphi}_{\mathrm{A}} \mathbf{d}_{I\mathrm{A}},\ \begin{Bmatrix} u_{II\mathrm{A}} \\ v_{II\mathrm{A}} \end{Bmatrix} = \boldsymbol{\varphi}_{\mathrm{A}} \mathbf{d}_{II\mathrm{A}}\right)_{local} \tag{31}$$

where

$$\begin{pmatrix} \mathbf{d}_{I\mathrm{A}} = \left\{\mathbf{d}_{I\mathrm{A}}^1 \quad \mathbf{d}_{I\mathrm{A}}^2 \quad \mathbf{d}_{I\mathrm{A}}^3 \quad \mathbf{d}_{I\mathrm{A}}^4 \quad \mathbf{d}_{I\mathrm{A}}^5 \quad \mathbf{d}_{I\mathrm{A}}^6\right\}^{\mathrm{T}} \\ \mathbf{d}_{II\mathrm{A}} = \left\{\mathbf{d}_{II\mathrm{A}}^1 \quad \mathbf{d}_{II\mathrm{A}}^2 \quad \mathbf{d}_{II\mathrm{A}}^3 \quad \mathbf{d}_{II\mathrm{A}}^4 \quad \mathbf{d}_{II\mathrm{A}}^5 \quad \mathbf{d}_{II\mathrm{A}}^6\right\}^{\mathrm{T}} \end{pmatrix}_{local} \tag{32}$$

and

$$\left(\begin{aligned} \mathbf{d}_{IA}^{i} &= \frac{1}{2}\left\{d_{A(2i-1)} + (-1)^{2i} d_{B(2i-1)},\quad d_{A(2i)} + (-1)^{2i-1} d_{B(2i)}\right\}^{T} \\ \mathbf{d}_{IIA}^{i} &= \frac{1}{2}\left\{d_{A(2i-1)} + (-1)^{2i-1} d_{B(2i-1)},\quad d_{A(2i)} + (-1)^{2i} d_{B(2i)}\right\}^{T} \end{aligned}\right)_{local}, i = 1, 2, \cdots, 6 \tag{33}$$

For six nodal points of one element, e.g. A_1, A_2, A_3, A_4, A_5 and A_6, we have

$$\left(\mathbf{u}_{IA} = \boldsymbol{\psi}_{A}\mathbf{d}_{IA}\right)_{local},\ \left(\mathbf{u}_{IIA} = \boldsymbol{\psi}_{A}\mathbf{d}_{IIA}\right)_{local} \tag{34}$$

where

$$\left(\begin{aligned} \mathbf{u}_{IA} &= \left(\mathbf{u}_{IA}^{1}\quad \mathbf{u}_{IA}^{2}\quad \mathbf{u}_{IA}^{3}\quad \mathbf{u}_{IA}^{4}\quad \mathbf{u}_{IA}^{5}\quad \mathbf{u}_{IA}^{6}\right)^{T} \\ \mathbf{u}_{IIA} &= \left(\mathbf{u}_{IIA}^{1}\quad \mathbf{u}_{IIA}^{2}\quad \mathbf{u}_{IIA}^{3}\quad \mathbf{u}_{IIA}^{4}\quad \mathbf{u}_{IIA}^{5}\quad \mathbf{u}_{IIA}^{6}\right)^{T} \end{aligned}\right)_{local} \tag{35}$$

and

$$\left(\begin{aligned} \mathbf{u}_{IA}^{i} &= \left\{u_{IA}^{i},\ v_{IA}^{i}\right\}^{T} \\ \mathbf{u}_{IIA}^{i} &= \left\{u_{IIA}^{i},\ v_{IIA}^{i}\right\}^{T} \end{aligned}\right)_{local}, i = 1, 2, \cdots, 6 \tag{36}$$

and

$$\left(\boldsymbol{\psi}_{A} = \left(\tilde{\boldsymbol{\varphi}}_{A}^{1}\quad \tilde{\boldsymbol{\varphi}}_{A}^{2}\quad \tilde{\boldsymbol{\varphi}}_{A}^{3}\quad \tilde{\boldsymbol{\varphi}}_{A}^{4}\quad \tilde{\boldsymbol{\varphi}}_{A}^{5}\quad \tilde{\boldsymbol{\varphi}}_{A}^{6}\right)^{T}\right)_{local} \tag{37}$$

where

$$\left((\tilde{\boldsymbol{\varphi}}_{A}^{i})^{T} = \begin{bmatrix} \varphi_{1A}^{i} & 0 & \varphi_{2A}^{i} & 0 & \varphi_{3A}^{i} & 0 & \varphi_{4A}^{i} & 0 & \varphi_{5A}^{i} & 0 & \varphi_{6A}^{i} & 0 \\ 0 & \varphi_{1A}^{i} & 0 & \varphi_{2A}^{i} & 0 & \varphi_{3A}^{i} & 0 & \varphi_{4A}^{i} & 0 & \varphi_{5A}^{i} & 0 & \varphi_{6A}^{i} \end{bmatrix}\right)_{local}, i = 1, 2, \cdots, 6 \tag{38}$$

and

$$\left(\begin{aligned} u_{IA}^{i} &= \frac{1}{2}(u_{A}^{i} + u_{B}^{i}),\ u_{IIA}^{i} = \frac{1}{2}(u_{A}^{i} - u_{B}^{i}) \\ v_{IA}^{i} &= \frac{1}{2}(v_{A}^{i} - v_{B}^{i}),\ v_{IIA}^{i} = \frac{1}{2}(v_{A}^{i} + v_{B}^{i}) \end{aligned}\right)_{local}, i = 1, 2, \cdots, 6 \tag{39}$$

From Eq. (34), one can obtain

$$\left(\mathbf{d}_{IA} = \boldsymbol{\psi}_{A}^{-1}\mathbf{u}_{IA}\right)_{local},\ \left(\mathbf{d}_{IIA} = \boldsymbol{\psi}_{A}^{-1}\mathbf{u}_{IIA}\right)_{local} \tag{40}$$

By using transformation matrix

$$\mathbf{T} = \mathrm{Diag}(\mathbf{t}, \mathbf{t}, \mathbf{t}, \mathbf{t}, \mathbf{t}, \mathbf{t}),\ \mathbf{t} = \begin{bmatrix} \cos\alpha & \sin\alpha \\ -\sin\alpha & \cos\alpha \end{bmatrix} \tag{41}$$

and “Diag()” represents diagonal matrix. Further, we have

$$\left(\mathbf{d}_{IA}\right)_{local} = \left(\boldsymbol{\psi}_{A}^{-1}\right)_{local}\mathbf{T}\left(\mathbf{u}_{IA}\right)_{global},\ \left(\mathbf{d}_{IIA}\right)_{local} = \left(\boldsymbol{\psi}_{A}^{-1}\right)_{local}\mathbf{T}\left(\mathbf{u}_{IIA}\right)_{global} \tag{42}$$

Eq. (42) is the so-called the decomposition of generalized degree of freedom. We can then calculate the energy release rate of the system as follows:

$$\left(G_I = -\frac{1}{2}\sum_{i=1}^{Nce}\mathbf{d}_{IA\,i}^{T}\frac{\partial \mathbf{k}_{Ai}}{b\partial l}\mathbf{d}_{IA\,i},\ G_{II} = -\frac{1}{2}\sum_{i=1}^{Nce}\mathbf{d}_{IIA\,i}^{T}\frac{\partial \mathbf{k}_{Ai}}{b\partial l}\mathbf{d}_{IIA\,i} \right)_{local} \tag{43}$$

where Nce is the number of crack-tip elements. The stress intensity factors K_I (mode-I) and K_{II} (mode-II) are then calculated by $K_I = \pm\sqrt{E^*G_I}$ and $K_{II} = \pm\sqrt{E^*G_{II}}$ respectively, in which $E^* = E$ for plane stress and $E^* = E/(1-\upsilon^2)$ for plane strain. E is the Young's modulus, and υ is the Poisson ratio. The signs of K_I and K_{II} are determined by examining the near crack-tip displacement according to their sign conventions.

Before 1995, as long as a combination of the VCET, SDT, and the DFDT were used to extract the SIFs of a mixed mode crack, symmetrical meshes or elements with respect to the *x*-axis of the local crack-tip coordinate system were almost always adopted. If the symmetrical meshes or elements were discarded, it is necessary to use an interpolation procedure for calculating the displacement of the mirror point B, as proposed in [28]. This is because point B is not always the nodal point of an element. Generally speaking, the interpolation procedure is one of the sources of the calculation error. In this study, this type of error is called the interpolation error. However, it is much more than this. Next, another source of the calculation error will be uncovered; unfortunately, this error source has been previously overlooked. It is enough to examine only the computational procedure of the energy release rate g_I of the crack-tip element ME_A, which contains the point A, see figure 9. g_I can be written as

$$\left(\begin{aligned} g_I &= -\frac{1}{2}\mathbf{d}_{IA}^{T}\frac{\partial \mathbf{k}_A}{b\partial l}\mathbf{d}_{IA} = -\frac{1}{2}\left[\left((\mathbf{d}_{IA}^{1})^{T},(\mathbf{d}_{IA}^{2})^{T},\cdots,(\mathbf{d}_{IA}^{6})^{T}\right)\right]\begin{bmatrix} \frac{\partial \mathbf{k}_{A1,1}}{b\partial l} & \frac{\partial \mathbf{k}_{A1,2}}{b\partial l} & \cdots & \frac{\partial \mathbf{k}_{A1,6}}{b\partial l} \\ \frac{\partial \mathbf{k}_{A2,1}}{b\partial l} & \frac{\partial \mathbf{k}_{A2,2}}{b\partial l} & \cdots & \cdots \\ \vdots & \vdots & \ddots & \cdots \\ \frac{\partial \mathbf{k}_{A6,1}}{b\partial l} & \cdots & \cdots & \frac{\partial \mathbf{k}_{A6,6}}{b\partial l} \end{bmatrix}\begin{pmatrix} \mathbf{d}_{IA}^{1} \\ \mathbf{d}_{IA}^{2} \\ \vdots \\ \mathbf{d}_{IA}^{6} \end{pmatrix} \\ &= -\frac{1}{2}\left[\left((\mathbf{d}_{IA}^{1})^{T}\frac{\partial \mathbf{k}_{A1,1}}{b\partial l} + (\mathbf{d}_{IA}^{2})^{T}\frac{\partial \mathbf{k}_{A2,1}}{b\partial l} + \cdots + (\mathbf{d}_{IA}^{6})^{T}\frac{\partial \mathbf{k}_{A6,1}}{b\partial l} + \cdots,\ \cdots \right)\right]\begin{pmatrix} \mathbf{d}_{IA}^{1} \\ \mathbf{d}_{IA}^{2} \\ \vdots \\ \mathbf{d}_{IA}^{6} \end{pmatrix} \end{aligned} \right)_{local} \tag{44}$$

where

$$\mathbf{k}_{Ai,j} = \begin{bmatrix} k_{Ai_1,j_1} & k_{Ai_1,j_2} \\ k_{Ai_2,j_1} & k_{Ai_2,j_2} \end{bmatrix}, i,j = 1,2,\cdots,6 \tag{45}$$

For the sake of brevity, considering only the first term (FT_A) of Eq. (44), it is

$$\left.\begin{cases} \mathrm{FT}_{\mathrm{A}} = -\dfrac{1}{2}\left(\left(\mathbf{d}_{IA}^{1}\right)^{\mathrm{T}}\dfrac{\partial\,\mathbf{k}_{\mathrm{A}1,1}}{b\partial\, l}\mathbf{d}_{IA}^{1}\right) = -\dfrac{1}{8b}\left(\left(d_{\mathrm{A}1}+d_{\mathrm{B}1}, d_{\mathrm{A}2}-d_{\mathrm{B}2}\right)\begin{bmatrix} \dfrac{\partial\, k_{\mathrm{A}1_1,1_1}}{\partial\, l} & \dfrac{\partial\, k_{\mathrm{A}1_1,1_2}}{\partial\, l} \\ \dfrac{\partial\, k_{\mathrm{A}1_2,1_1}}{\partial\, l} & \dfrac{\partial\, k_{\mathrm{A}1_2,1_2}}{\partial\, l}\end{bmatrix}\begin{pmatrix} d_{\mathrm{A}1}+d_{\mathrm{B}1} \\ d_{\mathrm{A}2}-d_{\mathrm{B}2}\end{pmatrix}\right) \\ \quad = \dfrac{1}{8b}\left(\underbrace{d_{\mathrm{A}1}\dfrac{\partial\, k_{\mathrm{A}1_1,1_1}}{\partial\, l}d_{\mathrm{A}1}}_{pure\ \ term} + \underbrace{d_{\mathrm{A}1}\dfrac{\partial\, k_{\mathrm{A}1_1,1_1}}{\partial\, l}d_{\mathrm{B}1} + d_{\mathrm{B}1}\dfrac{\partial\, k_{\mathrm{A}1_1,1_1}}{\partial\, l}d_{\mathrm{A}1} + d_{\mathrm{B}1}\dfrac{\partial\, k_{\mathrm{A}1_1,1_1}}{\partial\, l}d_{\mathrm{B}1}}_{mixed\ \ terms} + \cdots\right)\end{cases}\right)_{local} \tag{46}$$

Each of the crack-tip elements should take turns to play the role of element $\mathrm{ME_A}$ or element $\mathrm{ME_B}$. Similarly, for the crack-tip element $\mathrm{ME_B}$, which contains the point B, we have

$$\left.\begin{cases} \mathrm{FT}_{\mathrm{B}} = -\dfrac{1}{2}\left(\left(\mathbf{d}_{IB}^{1}\right)^{\mathrm{T}}\dfrac{\partial\,\mathbf{k}_{\mathrm{B}1,1}}{b\partial\, l}\mathbf{d}_{IB}^{1}\right) = -\dfrac{1}{8b}\left(\left(d_{\mathrm{B}1}+d_{\mathrm{A}1}, d_{\mathrm{B}2}-d_{\mathrm{A}2}\right)\begin{bmatrix} \dfrac{\partial\, k_{\mathrm{B}1_1,1_1}}{\partial\, l} & \dfrac{\partial\, k_{\mathrm{B}1_1,1_2}}{\partial\, l} \\ \dfrac{\partial\, k_{\mathrm{B}1_2,1_1}}{\partial\, l} & \dfrac{\partial\, k_{\mathrm{B}1_2,1_2}}{\partial\, l}\end{bmatrix}\begin{pmatrix} d_{\mathrm{B}1}+d_{\mathrm{A}1} \\ d_{\mathrm{B}2}-d_{\mathrm{A}2}\end{pmatrix}\right) \\ \quad = \dfrac{1}{8b}\left(\underbrace{d_{\mathrm{B}1}\dfrac{\partial\, k_{\mathrm{B}1_1,1_1}}{\partial\, l}d_{\mathrm{B}1}}_{pure\ \ term} + \underbrace{d_{\mathrm{B}1}\dfrac{\partial\, k_{\mathrm{B}1_1,1_1}}{\partial\, l}d_{\mathrm{A}1} + d_{\mathrm{A}1}\dfrac{\partial\, k_{\mathrm{B}1_1,1_1}}{\partial\, l}d_{\mathrm{B}1} + d_{\mathrm{A}1}\dfrac{\partial\, k_{\mathrm{B}1_1,1_1}}{\partial\, l}d_{\mathrm{A}1}}_{mixed\ \ terms} + \cdots\right)\end{cases}\right)_{local} \tag{47}$$

The mixed terms of Eqs. (46) and (47) mean that the generalized degree of freedom vector (for NMM) or the nodal displacement vector (for FEM) do not match the entries of the element stiffness matrix related to point A (or B). Taking the term $d_{\mathrm{B}1}\dfrac{\partial k_{\mathrm{B}1_1,1_1}}{\partial l}d_{\mathrm{A}1}$ as an example, in which $d_{\mathrm{B}1}$ and $k_{\mathrm{B}1_1,1_1}$ are all related to the $\mathrm{ME_B}$ containing the point B, whereas $d_{\mathrm{A}1}$ is related to the $\mathrm{ME_A}$ containing the point A. For the pure terms, however, that is not the case. When calculating the summation of the pure terms and mixed terms, these mixed terms are difficult to eliminate. This is believed to be another source of the calculation error. If asymmetric meshes or elements are used, the error is more significant. In this paper, this kind of error is called the mixed terms error. Perhaps the mixed terms error should receive more attention than the interpolation error. It should be pointed out that $\mathrm{FT_A}$ and $\mathrm{FT_B}$ should ultimately be counted up together.

Of course, these mixed terms can be regarded as a contribution to G_I or G_{II}; however, their physical meaning seem not to be so clear. In the following several paragraphs of this Section, we will demonstrate how the mixed terms error may be suppressed when using symmetrical meshes or elements. For this purpose, the nodal displacement vector will be employed based on several considerations. First, the initial VCET, SDT and DFDT stem from the FEM. Second, the nodal displacement vector is more physical meaning than the generalized degree of freedom vector in some cases. Taking the mode-I crack under uniform tension $\overline{t}$ as an example, see figure 10.

First, let us consider the partitioning of the element stiffness matrix corresponding to the six "stars" of the element $\mathrm{ME_A}$ and extract the following submatrix corresponding to "star" 1:

$$\left(\begin{bmatrix} \frac{\partial k_{A1_1,1_1}}{\partial l} & \frac{\partial k_{A1_1,1_2}}{\partial l} \\ \frac{\partial k_{A1_2,1_1}}{\partial l} & \frac{\partial k_{A1_2,1_2}}{\partial l} \end{bmatrix}\right)_{local} \quad (48)$$

The first term of the energy release rate can be expressed as

$$\left(\Lambda_{IA1} = -\frac{1}{2b}\left[\frac{1}{2}(u_{A1}+u_{B1}, v_{A1}-v_{B1})\right]\begin{bmatrix} \frac{\partial k_{A1_1,1_1}}{\partial l} & \frac{\partial k_{A1_1,1_2}}{\partial l} \\ \frac{\partial k_{A1_2,1_1}}{\partial l} & \frac{\partial k_{A1_2,1_2}}{\partial l} \end{bmatrix}\begin{pmatrix} \frac{1}{2}(u_{A1}+u_{B1}) \\ \frac{1}{2}(v_{A1}-v_{B1}) \end{pmatrix}\right)_{local} \quad (49)$$

In this example, we have

$$\left(u_{B1} = u_{A1},\ v_{B1} = -v_{A1}\right)_{local} \quad (50)$$

Thus, for point A1, we can obtain

$$\left(u_{IA1} = u_{A1}, v_{IA1} = v_{A1}\right)_{local} \quad (51)$$

Hence, Eq. (49) becomes

$$\left(\Lambda_{IA1} = -\frac{1}{2b}(u_{A1}, v_{A1})\begin{bmatrix} \frac{\partial k_{A1_1,1_1}}{\partial l} & \frac{\partial k_{A1_1,1_2}}{\partial l} \\ \frac{\partial k_{A1_2,1_1}}{\partial l} & \frac{\partial k_{A1_2,1_2}}{\partial l} \end{bmatrix}\begin{pmatrix} u_{A1} \\ v_{A1} \end{pmatrix}\right)_{local} \quad (52)$$

Whereas for point B1, Eq. (51) can be written as

$$\left(u_{IB1} = u_{A1}, v_{IB1} = -v_{A1}\right)_{local} \quad (53)$$

Similarly, for point B1 we can obtain

$$\left(\Lambda_{IB1} = -\frac{1}{2b}(u_{A1}, -v_{A1})\begin{bmatrix} \frac{\partial k_{B1_1,1_1}}{\partial l} & \frac{\partial k_{B1_1,1_2}}{\partial l} \\ \frac{\partial k_{B1_2,1_1}}{\partial l} & \frac{\partial k_{B1_2,1_2}}{\partial l} \end{bmatrix}\begin{pmatrix} u_{A1} \\ -v_{A1} \end{pmatrix} = -\frac{1}{2b}(u_{A1}, v_{A1})\begin{bmatrix} \frac{\partial k_{B1_1,1_1}}{\partial l} & -\frac{\partial k_{B1_1,1_2}}{\partial l} \\ -\frac{\partial k_{B1_2,1_1}}{\partial l} & \frac{\partial k_{B1_2,1_2}}{\partial l} \end{bmatrix}\begin{pmatrix} u_{A1} \\ v_{A1} \end{pmatrix}\right)_{local} \quad (54)$$

Summing Eqs. (52) and (54), we have

$$\left(\Lambda_{IA1} + \Lambda_{IB1} = -\frac{1}{2b}(u_{A1}, v_{A1})\left\{\begin{bmatrix} \frac{\partial k_{A1_1,1_1}}{\partial l} & \frac{\partial k_{A1_1,1_2}}{\partial l} \\ \frac{\partial k_{A1_2,1_1}}{\partial l} & \frac{\partial k_{A1_2,1_2}}{\partial l} \end{bmatrix} + \begin{bmatrix} \frac{\partial k_{B1_1,1_1}}{\partial l} & -\frac{\partial k_{B1_1,1_2}}{\partial l} \\ -\frac{\partial k_{B1_2,1_1}}{\partial l} & \frac{\partial k_{B1_2,1_2}}{\partial l} \end{bmatrix}\right\}\begin{pmatrix} u_{A1} \\ v_{A1} \end{pmatrix}\right)_{local} \quad (55)$$

On the other hand, for a "star", a following 2×2 submatrix (Eq. (56)) came from the element stiffness matrix $(\mathbf{k}_A)_{local}$ corresponding to the element ME_A, which contains the point A.

$$\left(\begin{bmatrix} k_{\mathrm{A}\,i_1,j_1} & k_{\mathrm{A}\,i_1,j_2} \\ k_{\mathrm{A}\,i_2,j_1} & k_{\mathrm{A}\,i_2,j_2} \end{bmatrix}\right)_{local}, i, j = 1, 2, \cdots, 6 \tag{56}$$

under the condition that the two elements are symmetrical with respect to the *x*-axis of the local crack-tip coordinate system, in the element stiffness matrix $(\mathbf{k}_{\mathrm{B}})_{local}$ corresponding to the element $\mathrm{ME_B}$, which contains the point B, a 2×2 submatrix

$$\left(\begin{bmatrix} k_{\mathrm{B}\,m_1,n_1} & k_{\mathrm{B}\,m_1,n_2} \\ k_{\mathrm{B}\,m_2,n_1} & k_{\mathrm{B}\,m_2,n_2} \end{bmatrix}\right)_{local}, m, n = 1, 2, \cdots, 6 \tag{57}$$

can always be found and make the following relationships hold

$$\left(\begin{bmatrix} k_{\mathrm{A}\,i_1,j_1} & k_{\mathrm{A}\,i_1,j_2} \\ k_{\mathrm{A}\,i_2,j_1} & k_{\mathrm{A}\,i_2,j_2} \end{bmatrix} = \begin{bmatrix} k_{\mathrm{B}\,m_1,n_1} & -k_{\mathrm{B}\,m_1,n_2} \\ -k_{\mathrm{B}\,m_2,n_1} & k_{\mathrm{B}\,m_2,n_2} \end{bmatrix}\right)_{local} \tag{58}$$

For matrix $(\partial \mathbf{k}_{\mathrm{A}} / \partial l)_{local}$ deriving from Eq. (20), a similar relationship can also exist. On the premise of using the simplex integration, Eq. (58) can be verified easily by symbolic operation system such as MATLAB, Maple or Mathmatics. In the Appendix, taking the three-node triangular mesh as an example, a relaxed proof is given. Due to Eq. (58), Eq. (55) becomes

$$\left(\Lambda_{I\mathrm{A}1} + \Lambda_{I\mathrm{B}1} = -\frac{1}{b}\left(u_{\mathrm{A}1}, v_{\mathrm{A}1}\right)\left\{\begin{bmatrix} \dfrac{\partial k_{\mathrm{A}1_1,1_1}}{\partial l} & \dfrac{\partial k_{\mathrm{A}1_1,1_2}}{\partial l} \\ \dfrac{\partial k_{\mathrm{A}1_2,1_1}}{\partial l} & \dfrac{\partial k_{\mathrm{A}1_2,1_2}}{\partial l} \end{bmatrix}\right\}\begin{pmatrix} u_{\mathrm{A}1} \\ v_{\mathrm{A}1} \end{pmatrix}\right)_{local} \tag{59}$$

From Eq. (59) it can be seen that, when there are symmetrical meshes or elements with respect to the *x*-axis of the local crack-tip coordinate system, the mixed terms of mode-I crack are absent in quantitative terms. For the mode-II crack the same conclusions can be obtained and need not be repeated here. These conclusions can also be applied to numerical integration because numerical integration is an approximate of analytic integration.

5. EXTRACTION OF STRESS INTENSITY FACTORS

In this section, we validate the proposed methods by comparing the numerical results to the existing theoretical ones. Only in the first example, are the symmetrical and asymmetrical configurations with respect to the *x*-axis of the local crack-tip coordinate system adopted to demonstrate the necessity of using the symmetrical configuration in order to improve the computational accuracy. And only in the same example, are the finite difference approximation and the proposed analytic expression of the energy release rate used to compare the calculation accuracy. In the rest examples, the unsymmetrical configuration and the finite difference approximation are not all considered.

5.1 Edge-cracked plate under mode-I loading

In this example, a finite plate with an edge crack under uniaxial tension is investigated, as shown in figure 11(a). The reference K_I was given by Ewalds et al. [72]

$$K_I = F\sigma\sqrt{\pi a} \tag{60}$$

where F is a modification factor to reflect the size effect, and a is the length of the crack. If $a/W \le 0.6$, approximated by

$$F = 1.12 - 0.231\left(\frac{a}{W}\right) + 10.55\left(\frac{a}{W}\right)^2 - 21.72\left(\frac{a}{W}\right)^3 + 30.39\left(\frac{a}{W}\right)^4 \tag{61}$$

The width and height of the plate are given by W = 1.0m and H = 2.0m, respectively. A plane stress condition is assumed with E = 207,000Pa, $\upsilon = 0.30$. The far-field tensile stress is given by $\sigma = 1.0\,\mathrm{N/m^2}$. The local mathematical cover refinement (LMCR) is adopted near the crack-tip.

The K_I of plates with different crack lengths ranging from a = 0.1 to 0.6m are calculated. Seventeen layers of triangular meshes with LMCR near the crack-tip are used. At the same time, to show the the necessity of using the symmetrical configuration, the asymmetrical and symmetrical configurations with respect to the x-axis of the local crack-tip coordinate system are adopted, as shown in figure 12 for the case of a = 0.1m. For the case of the asymmetrical configuration, some results are listed in Table I.

From Table I, we can see that for the different a the calculation values obtained by finite difference approximation are gradually close to the reference along with the reduction of the value of scale. At the same time, we can find that the calculation values given by the proposed analytic expression have a better precision.

On the other hand, for the case of the symmetrical configuration with respect to the x-axis of the local crack-tip coordinate system, some results are listed in Table II.

For the different a , similar to the case of asymmetrical configuration with respect to the x-axis of the local crack-tip coordinate system, from Table II, it is can be observed that the more the value of scale decrease, the more the calculation value obtained by finite difference approximation is close to the reference. For the proposed analytic expression, however, the precision of the calculation value is more satisfying, namely, the relative error are all less than 0.83%. Further, when the proposed analytic expression is adopted the REs of K_I obtained by using asymmetrical and symmetrical configuration are shown in figure 13. It is apparent that the accuracy corresponding to symmetrical configuration is better than that corresponding to asymmetrical configuration.

5.2. Homogenous infinite plate with a central crack

In figure14, the homogeneous plate containing a central crack (line segment AB) is considered; where $W = H = 200$mm and $a = 10$mm, and the thickness of the plate is 1mm. Because $W/a = H/a = 20$, the plate can be considered as an infinite one. The material constants are given by $E = 210$MPa, $\upsilon = 0.28$. A plane stress condition is assumed. In theory $K_{II} = \tau\sqrt{\pi a} = 3.963327 \mathrm{N\,mm}^{-1.5}$ when $\tau = 1$ MPa. During the numerical simulation, the layer numbers (LNs) of the triangular mesh with the LMCR range from 16 to 20 with an interval of 2. The calculated K_{II} for different LNs are listed in Table III. It can easily be seen that when the MC is gradually refined, K_{II} converges to the theoretical solution, and when LNs = 20, the RE is within 0.84%.

5.3. Edge-cracked plate under mixed mode loading

This example involves an edge-cracked plate in figure 15, which is fixed at the bottom and subjected to far-field shear stress $\tau = 1.0\ \mathrm{N/m^2}$ at the top. The width and height of the plate are given by $W = 7.0$m and $H = 16.0$m, respectively. The crack length is given by $a = 3.5$m. A plane strain condition is assumed. The elastic modulus and Poisson ratio are given by $E = 30$MPa and $\upsilon = 0.25$ respectively. During the numerical calculation, the LNs of triangular mesh range from 12 to 24 with an interval of 2; the LMCR is also used. The calculated K_I and K_{II} for different LNs are listed in Table IV. It can easily be seen that, when the MC is gradually refined, K_I and K_{II} both converge to the reference solutions, and when LNs = 24, the relative errors are within 1.15% and 1.07% for K_I and K_{II} respectively.

Further, the curves of relative error of K_I and K_{II} vs. DOF are shown in figures 16 and 17, respectively, as well as the relative error given by Giner et al. [39]. For the purpose of comparison, the opposite number of the relative error given by this study is used in the two figures in order to be consistent with Giner et al. [39].

From figures 16, for the K_I of this example, the convergence rate and relative errors obtained by the proposed method seems to be slightly faster and slightly more than that given by the method [39] respectively. Whereas, the relative errors obtained by the two methods are all approximate zero along with the increasement of DOF. For the K_{II} of this example, as we can see from figure 17, the two methods have roughly the same convergence rate. And the relative error obtained by the proposed method is slightly lower than the one given by the other method. However, considering the following two points: one, both methods all use analytic expression for the stiffness derivative. Thus, the truncation error caused by the difference approximation can be avoided; two, the symmetrical mathematic cover with respect to the x-axis of the local crack-tip coordinate system is employed by this study. Therefore, the interpolation error and the mixed terms error cannot be involved. The h-adaptive refinement utilized by [39] can achieve the same effect. And we have reasons to believe that the difference will be smaller if the number of DOF is further increased.

5.4. Square plate with an inclined center crack subjected to tension

A square plate with an inclined center crack subjected to uniform tension is considered in figure 18. The plate has a dimensions of $W = H = 10.0$m, half crack length of $a = 1.0$m, and the uniform tension σ is taken to be unity. The reference solution is [73]

$$K_I = \sigma\sqrt{\pi a}\cos^2\beta,\ K_{II} = \sigma\sqrt{\pi a}\sin\beta\cos\beta \tag{62}$$

The material constants are given by E = 210MPa and $\upsilon = 0.28$ respectively, and a plane stress condition is assumed. During the simulation, six inclined angles, i.e. β = 0°, 15°, 30°, 45°, 60° and 75°, are examined.

Taking the case of β = 60° as an example, six different discrete models with 652, 810, 1062, 1236, 1512, and 1782 elements are adopted to examine the trend of convergence of the proposed methods. The results are listed in Table V, from which we can see that the more the number of elements, the higher the precision. In addition, figure 19 shows the normalized K_I and K_{II} with different the number of elements. It can be observed that the normalized K_I and K_{II} are all tend to "1" along with the increment of the number of elements.

Thirty layers of triangular meshes with LMCR near the crack-tips are always used for all of the cases. The SIFs are plotted in figure 20. The results obtained by the present methods agree well with the reference solutions.

Like XFEM [17, 18], the tip or discontinuous enrichment function was also employed by NMM in [74]. The results obtained by the proposed methods and that given by using tip enrichment function [74] are shown in figure 21. As we can see, these calculation results can be considered to be similar. For this example, it is worth mentioning that about 3560 elements are adopted by [74]; whereas, in this study, because the LMCR is used, the maximum of the number of elements is reduced to about 1800 (see Table V) to achieve the acceptable accuracy.

6. CONCLUSION

This work was devoted to the establishment of a technique aiming to decompose the generalized degrees of freedom for mixed-mode crack problems. The new technique is tailor-made for the cover-based methods or for the methods involving the generalized degree of freedom. In addition, by means of the virtual crack extension technique and the simplex integration method, an analytic expression of the energy release rate or the stiffness derivative was obtained. The analytic expression can also evade the error, which is caused by the difference approximation. Moreover, when the decomposition technique of generalized degrees of freedom or the displacement field decomposition technique is used to extract stress intensity factors, a detailed analysis was given to show that it is necessary to adopt symmetric meshes or elements with respect to the horizontal axis of the local crack-tip coordinate system. Furthermore, the local mathematical cover refinement was further applied in the high-order NMM. The implementation of the local mathematical cover refinement is expected to be the basis of an h-version of NMM. The validity of the proposed methods was verified by comparing the numerical solutions with the analytical ones.

APPENDIX

Proposition. In three-node triangular mesh-based NMM, for any submatrix of $\mathbf{k}_{\mathrm{A}}$ corresponding to the three “stars” of any element $\mathrm{ME_A}$

$$\begin{bmatrix} k_{\mathrm{A}\,i_1,j_1} & k_{\mathrm{A}\,i_1,j_2} \\ k_{\mathrm{A}\,i_2,j_1} & k_{\mathrm{A}\,i_2,j_2} \end{bmatrix}, \; i,j=1,2,3 \tag{A1}$$

under the condition that the elements $\mathrm{ME_A}$, $\mathrm{ME_B}$ and the triangular meshes covering them are symmetrical with respect to the *x*-axis of the local crack-tip coordinate system, in matrix $\mathbf{k}_{\mathrm{B}}$, a submatrix

$$\begin{bmatrix} k_{\mathrm{B}\,m_1,n_1} & k_{\mathrm{B}\,m_1,n_2} \\ k_{\mathrm{B}\,m_2,n_1} & k_{\mathrm{B}\,m_2,n_2} \end{bmatrix}, \; m,n=1,2,3 \tag{A2}$$

can always be found and make the following relationships hold

$$\begin{bmatrix} k_{\mathrm{A}\,i_1,j_1} & k_{\mathrm{A}\,i_1,j_2} \\ k_{\mathrm{A}\,i_2,j_1} & k_{\mathrm{A}\,i_2,j_2} \end{bmatrix} = \begin{bmatrix} k_{\mathrm{B}\,m_1,n_1} & -k_{\mathrm{B}\,m_1,n_2} \\ -k_{\mathrm{B}\,m_2,n_1} & k_{\mathrm{B}\,m_2,n_2} \end{bmatrix} \tag{A3}$$

Proof. Considering element $\mathrm{ME_A}$ and triangle $\Delta 123$ covering $\mathrm{ME_A}$ are shown in figure A1, where point $\mathrm{A_1}$, $\mathrm{A_2}$ and $\mathrm{A_3}$ are the three nodes of the $\mathrm{ME_A}$, whereas points 1, 2 and 3 are the three “stars”. Manifold element $\mathrm{ME_B}$ and triangle $\Delta 2^*1^*3^*$ are the symmetry geometries of $\mathrm{ME_A}$ and $\Delta 123$, respectively. Points $\mathrm{B_1}$, $\mathrm{B_2}$ and $\mathrm{B_3}$ are the three nodes of $\mathrm{ME_B}$, whereas points 1*, 2* and 3* are the three “stars”.

1. For any point $(x_{\mathrm{A}}, y_{\mathrm{A}})$ in $\Delta 123$, of cause point $(x_{\mathrm{A}}, y_{\mathrm{A}})$ is also inside of element $\mathrm{ME_A}$, we define

$$L_{k\mathrm{A}} = \frac{a_{k\mathrm{A}} + b_{k\mathrm{A}} x_{\mathrm{A}} + c_{k\mathrm{A}} y_{\mathrm{A}}}{2\Delta_{\mathrm{A}}}, \quad k=1,2,3 \tag{A4}$$

where

$$\Delta_{\mathrm{A}} = \frac{1}{2} \det \begin{bmatrix} 1 & s_1 & t_1 \\ 1 & s_2 & t_2 \\ 1 & s_3 & t_3 \end{bmatrix} \tag{A5}$$

and

$$a_{1\mathrm{A}} = s_2 t_3 - s_3 t_2, \quad b_{1\mathrm{A}} = t_2 - t_3, \quad c_{1\mathrm{A}} = s_3 - s_2 \tag{A6}$$

with cyclic rotation of indices 1, 2, and 3. $(s_1,t_1),(s_2,t_2)$ and (s_3,t_3) are the coordinates of “stars” 1, 2 and 3, respectively. The corresponding partition of unity is

$$\varphi_{1A} = L_{1A}, \quad \varphi_{2A} = L_{2A}, \quad \varphi_{3A} = L_{3A} \tag{A7}$$

In matrix form, it is

$$\begin{pmatrix} \varphi_{1A} \\ \varphi_{2A} \\ \varphi_{3A} \end{pmatrix} = \begin{pmatrix} f_{11A} & f_{12A} & f_{13A} \\ f_{21A} & f_{22A} & f_{23A} \\ f_{31A} & f_{32A} & f_{33A} \end{pmatrix} \begin{pmatrix} 1 \\ x_A \\ y_A \end{pmatrix} \tag{A8}$$

where

$$f_{i1A} = \frac{a_{iA}}{2\Delta_A}, \; f_{i2A} = \frac{b_{iA}}{2\Delta_A}, \quad f_{i3A} = \frac{c_{iA}}{2\Delta_A}, \; i = 1,2,3 \tag{A9}$$

2. For any point (x_B, y_B) in $\Delta 2^* 1^* 3^*$, we define

$$L_{kB} = \frac{a_{kB} + b_{kB} x_B + c_{kB} y_B}{2\Delta_B}, \quad k = 1,2,3 \tag{A10}$$

where (please note the small differences from Eq.(A5).)

$$\Delta_B = \frac{1}{2} \det \begin{bmatrix} 1 & s_2^* & t_2^* \\ 1 & s_1^* & t_1^* \\ 1 & s_3^* & t_3^* \end{bmatrix} \tag{A11}$$

and (please note the small differences from Eq. (A6).)

$$a_{1B} = s_1^* t_3^* - s_3^* t_1^*, \; b_{1B} = t_1^* - t_3^*, \; c_{1B} = s_3^* - s_1^* \tag{A12}$$

with cyclic rotation of indices 1*, 2* and 3*. Where $(s_1^*, t_1^*), (s_2^*, t_2^*)$ and (s_3^*, t_3^*) are the coordinates of "stars" 1*, 2* and 3* respectively. The corresponding partition of unity is

$$\varphi_{1B} = L_{1B}, \quad \varphi_{2B} = L_{2B}, \quad \varphi_{3B} = L_{3B} \tag{A13}$$

In matrix form, it is

$$\begin{pmatrix} \varphi_{1B} \\ \varphi_{2B} \\ \varphi_{3B} \end{pmatrix} = \begin{pmatrix} f_{11B} & f_{12B} & f_{13B} \\ f_{21B} & f_{22B} & f_{23B} \\ f_{31B} & f_{32B} & f_{33B} \end{pmatrix} \begin{pmatrix} 1 \\ x_B \\ y_B \end{pmatrix} \tag{A14}$$

where

$$f_{i1B} = \frac{a_{iB}}{2\Delta_B}, \; f_{i2B} = \frac{b_{iB}}{2\Delta_B}, \quad f_{i3B} = \frac{c_{iB}}{2\Delta_B}, \; i = 1,2,3 \tag{A15}$$

Due to the symmetry, it is the case that

$$\begin{Bmatrix} x_B \\ y_B \end{Bmatrix} = \begin{Bmatrix} x_A \\ -y_A \end{Bmatrix}, \begin{Bmatrix} s_i \\ t_i \end{Bmatrix} = \begin{Bmatrix} s_i^* \\ -t_i^* \end{Bmatrix}, \; i = 1,2,3 \tag{A16}$$

Thus, we have

$$\Delta_{\mathrm{B}} = \Delta_{\mathrm{A}}, a_{i\mathrm{B}} = a_{i\mathrm{A}},\ b_{i\mathrm{B}} = b_{i\mathrm{A}},\ c_{i\mathrm{B}} = -c_{i\mathrm{A}},\quad i = 1,2,3 \tag{A17}$$

Further, one can obtain

$$f_{i1\mathrm{B}} = f_{i1\mathrm{A}},\ f_{i2\mathrm{B}} = f_{i2\mathrm{A}},\ f_{i3\mathrm{B}} = -f_{i3\mathrm{A}},\quad i = 1,2,3 \tag{A18}$$

3. Considering the following submatrix

$$\mathbf{k}_{ij} = \int_{\Omega^e} \left(\mathbf{B}_i\right)^{\mathrm{T}} \mathbf{D}\mathbf{B}_j \mathrm{d}\Omega,\quad i, j = 1,23 \tag{A19}$$

where $\mathbf{D}$ is the elasticity matrix and Ω^e is the domain occupied by an element. The entries of the strain-displacement matrix $\mathbf{B}_i$ are

$$\mathbf{B}_i = \begin{bmatrix} f_{i2} & 0 \\ 0 & f_{i3} \\ f_{i3} & f_{i2} \end{bmatrix},\ i = 1,2,3 \tag{A20}$$

Because $\mathbf{D}$ is a symmetric constant matrix and does not affect the desired conclusion in this Appendix, we will adopt the following expression to simplify

$$\mathbf{k}^*_{ij} = \int_{\Omega^e} \left(\mathbf{B}_i\right)^{\mathrm{T}} \mathbf{B}_j \mathrm{d}\Omega,\quad i, j = 1,23 \tag{A21}$$

and we have

$$\mathbf{k}^*_{ij} = \int_{\Omega^e} \left(\mathbf{B}_i\right)^{\mathrm{T}} \mathbf{B}_j \mathrm{d}\Omega = \int_{\Omega^e} \begin{bmatrix} f_{i2} & 0 & f_{i3} \\ 0 & f_{i3} & f_{i2} \end{bmatrix} \begin{bmatrix} f_{j2} & 0 \\ 0 & f_{j3} \\ f_{j3} & f_{j2} \end{bmatrix} \mathrm{d}\Omega = \Delta^e \begin{bmatrix} f_{i2} f_{j2} + f_{i3} f_{j3} & f_{i3} f_{j2} \\ f_{i2} f_{j3} & f_{i3} f_{j3} + f_{i2} f_{j2} \end{bmatrix} \tag{A22}$$

where Δ^e is the area of an element. Using Eq. (A18), for elements $\mathrm{ME_A}$ and $\mathrm{ME_B}$, according to the following one-to-one correspondence

$$\begin{aligned} &\mathbf{k}^*_{\mathrm{A}1,1} \to \mathbf{k}^*_{\mathrm{B}2,2},\ \mathbf{k}^*_{\mathrm{A}1,2} \to \mathbf{k}^*_{\mathrm{B}2,1},\ \mathbf{k}^*_{\mathrm{A}1,3} \to \mathbf{k}^*_{\mathrm{B}2,3} \\ &\mathbf{k}^*_{\mathrm{A}2,1} \to \mathbf{k}^*_{\mathrm{B}1,2},\ \mathbf{k}^*_{\mathrm{A}2,2} \to \mathbf{k}^*_{\mathrm{B}1,1},\ \mathbf{k}^*_{\mathrm{A}2,3} \to \mathbf{k}^*_{\mathrm{B}1,3} \\ &\mathbf{k}^*_{\mathrm{A}3,1} \to \mathbf{k}^*_{\mathrm{B}3,2},\ \mathbf{k}^*_{\mathrm{A}3,2} \to \mathbf{k}^*_{\mathrm{B}3,1},\ \mathbf{k}^*_{\mathrm{A}3,3} \to \mathbf{k}^*_{\mathrm{B}3,3} \end{aligned} \tag{A23}$$

the following relationships are always valid:

$$\begin{bmatrix} k^*_{\mathrm{A}\,i_1,j_1} & k^*_{\mathrm{A}\,i_1,j_2} \\ k^*_{\mathrm{A}\,i_2,j_1} & k^*_{\mathrm{A}\,i_2,j_2} \end{bmatrix} = \begin{bmatrix} k^*_{\mathrm{B}\,m_1,n_1} & -k^*_{\mathrm{B}\,m_1,n_2} \\ -k^*_{\mathrm{B}\,m_2,n_1} & k^*_{\mathrm{B}\,m_2,n_2} \end{bmatrix},\ i, j, m, n = 1,2,3 \tag{A24}$$

Hence, the abovementioned proposition is proved. □

ACKNOWLEDGEMENT

This study is supported by the National Basic Research Program of China (Grant nos. 2011CB013505 and 2014CB047100), the National Natural Science Foundation of China (Grant nos. 11572009 and 41272346).

REFERENCES

[1] Irwin GR. Analysis of stresses and strains near the end of a crack traversing a plate. *Journal of Applied Mechanics*. 1957; **24**:361–364.

[2] Griffith AA. The phenomena of rupture and flow in solids. *Philosophical Transactions of the Royal Society of London*. 1921; **A211**:163–198.

[3] Rice JR. A path independent integral and the approximation analysis of strain concentration by notches and cracks. *Journal of Applied Mechanics*. 1968; **35**:379–386.

[4] Chan SK, Tuba IS, Wilson WK. On the finite element method in linear fracture mechanics. *Engineering Fracture Mechanics*. 1970; **2**:1–17.

[5] Henshell RD, Shaw KG. Crack tip finite elements are unnecessary. *International Journal for Numerical Methods in Engineering*. 1975; **9**:495–507.

[6] Barsoum RS. Triangular quarter-point elements as elastic and perfectly-plastic crack tip elements. *International Journal for Numerical Methods in Engineering*. 1977; **11**:85–98.

[7] Hussain MA, Coffin LF, Zaleski KA. Three dimensional singular elements. *Computers & Structures*. 1981; **13**:595–599.

[8] Irwin GR. Analysis of stresses and strains near the end of a crack traversing a plate. *Journal of Applied Mechanics*. 1957; **24**:361–364.

[9] Rybicki EF, Kanninen MF. A finite element calculation of stress intensity factors by a modified crack closure integral. *Engineering Fracture Mechanics*. 1977; **9**:931–938.

[10] Kim JH, Paulino GH. Finite element evaluation of mixed mode stress intensity factors in functionally graded materials. *International Journal for Numerical Methods in Engineering*. 2002; **53**:1903–1935.

[11] Ishikawa H, Kitagawa H, Okamura H. J integral of a mixed mode crack and its application. *In proceedings of 3rd International Conference on Mechanics Behavior of Material*. 1979; **3**:447–455.

[12] Li FZ, Shih CF, Needleman A. A comparison of methods for calculating energy release rates. *Engineering Fracture Mechanics*. 1985; **21**(2):405–421.

[13] Raju IS, Shivakumar KN. An equivalent domain integral method in the two-dimensional analysis of mixed mode crack problems. *Engineering Fracture Mechanics*. 1990; **37**(4):707–725.

[14] Yau JF, Wang SS, Corten HT. A mixed-mode crack analysis of isotropic solids using conservation laws of elasticity. *Journal of Applied Mechanics*. 1980; **47**:335–341.

[15] Shih CF, Asaro RJ. Elastic-plastic analysis of cracks on bimaterial interfaces: Part I—small scale yielding. *Journal of Applied Mechanics*. 1988; **55**:299–318.

[16] Fleming M, Chu YA, Moran B, Belytschko T. Enriched element-free Galerkin methods for singular fields. Internat. *International Journal for Numerical Methods in Engineering*. 1997; **40**:1483–1504.

[17] Belytschko T, Black T. Elastic crack growth in finite elements with minimal remeshing. *Internat. International Journal for Numerical Methods in Engineering*. 1999; **45**:601–620.

[18] Moes N, Dolbow J, Belystchko T. A finite element method for crack growth without remeshing. *International Journal for Numerical Methods in Engineering*. 1999; **46**:131–150.

[19] Waisman H. An analytical stiffness derivative extended finite element technique for extraction of crack tip strain energy release rates. *Engineering Fracture Mechanics*. 2010; **77**(16):3204–3215.

[20] Lan M, Waisman H, Harari I. A direct analytical method to extract mixed-mode components of strain energy release rates from Irwin's integral using extended finite element method. *International Journal for Numerical Methods in Engineering*. 2013; **95**(12):1033–1052.

[21] Lan M, Waisman H, Harari I. A High-order extended finite element method for extraction of mixed-mode strain energy release rates in arbitrary crack settings based on Irwin's integral. *International Journal for Numerical Methods in Engineering*. 2013; **96**(12):787–812.

[22] Song G, Waisman H, Lan M, et al. Extraction of stress intensity factors from Irwin's integral using high-order XFEM on triangular meshes. *International Journal for Numerical Methods in Engineering*. 2015; **102**(3-4):528–550.

[23] Parks DM. A stiffness derivative finite element technique for determination of crack tip stress intensity factors. *International Journal of Fracture*. 1974; **10**(4):487–502.

[24] Hellen TK. On the method of virtual crack extensions. *International Journal for Numerical Methods in Engineering*. 1975; **9**:187–207.

[25] Nikishkov GP, Vainshtok VA. Method of virtual crack growth for determining stress intensity factors KI and KII. *Translated from Problemy Prochnosti*. 1980; **6**:26–30.

[26] Ishikawa H. A finite element analysis of stress intensity factors for combined tensile and shear loading by only a virtual crack extension. *International Journal of Fracture*. 1980; **16**:243–246.

[27] Suo XZ, Combescure A. Double virtual crack extension method for crack growth stability assessment. *International Journal of Fracture*. 1992; **57**:127–150.

[28] Xie M, Gerstle WH, Rahulkumar P. Energy-based automatic mixed-mode crack-propagation modeling. *Journal of Engineering Mechanics*. 1995; **12**:914–923.

[29] Glodez S, Ren Z. Modelling of crack growth under cyclic contact loading. *Theoretical and Applied Fracture Mechanics*. 1998; **30**:159–173.

[30] Flasker J, Fajdiga G, Glodez S, Hellen TK. Numerical simulation of surface pitting due to contact loading. *International Journal of Fatigue*. 2001; **23**:599–605.

[31] Delorenzi HG. On the energy release rate and the J-integral for 3-D crack configurations. *International Journal of Fracture*. 1982; **19**:183–193.

[32] Haber RB, Koh HM. Explicit expressions for energy release rates using virtual crack extensions. *International Journal for Numerical Methods in Engineering*. 1985; **21**:301–35.

[33] Lin SC, Abel JF. Variational approach for a new direct-integration form of the virtual crack extension

method. *International Journal of Fracture*. 1988; **38**:217–235.

[34] Davis BR, Wawrzynek PA, Hwang CG, Ingraffea AR. Decomposition of 3-D mixed-mode energy release rates using the virtual crack extension method. *Engineering Fracture Mechanics*. 2014; **131**:382–405.

[35] Komkov V, Choi KK, Haug EJ. Design sensitivity analysis of structural systems. Academic press, New York, NY. 1986.

[36] Feijóo RA, Padra C, Saliba R, et al. Shape sensitivity analysis for energy release rate evaluation and its application to the study of three-dimensional cracked bodies. *Computer methods in applied mechanics and engineering*. 2000; **188**(4):649–664.

[37] Chen G, Rahman S, Park YH. Shape sensitivity and reliability analyses of linear-elastic cracked structures. *International Journal of Fractur*e. 2001a; **112**(3):223–246.

[38] Chen G, Rahman S, Park YH. Shape sensitivity analysis in mixed-mode fracture mechanics. *Computational Mechanics*. 2001b; **27** (4):282–291.

[39] Giner E, Fuenmayor FJ, Besa AJ, et al. An implementation of the stiffness derivative method as a discrete analytical sensitivity analysis and its application to mixed mode in LEFM. *Engineering fracture mechanics*. 2002; **69**(18):2051–2071.

[40] Giner E, Fuenmayor FJ, Baeza L, et al. Error estimation for the finite element evaluation of G_I and G_{II} in mixed-mode linear elastic fracture mechanics. *Finite Elements in Analysis and Design*. 2005; **41**(11):1079–1104.

[41] Giner E, Fuenmayor FJ, Tarancón JE. An improvement of the EDI method in linear elastic fracture mechanics by means of an a posteriori error estimator in G. *International journal for numerical methods in engineering*. 2004; **59**(4):533–558.

[42] Van Miegroet L, Duysinx P. Stress concentration minimization of 2D filets using X-FEM and level set description. *Structural and Multidisciplinary Optimization*. 2007; **33**(4–5):425–438.

[43] Van Miegroet L. Generalized shape optimization using XFEM and level set description. Ph.D. Thesis, University of Liège, Liège, 2012.

[44] Rao BN, Rahman S. A continuum shape sensitivity method for fracture analysis of isotropic functionally graded materials. *Computational Mechanics*. 2006; **38**:133–150.

[45] Rao BN, Rahman S. A continuum shape sensitivity method for fracture analysis of orthotropic functionally graded materials. *Mechanics of Materials*. 2005; **37**(10):1007–1025.

[46] Osher S, Sethian JA. Fronts propagating with curvature-dependent speed: algorithms based on Hamilton-Jacobi formulations. *Journal of Computational Physics*. 1988; **79**(1):12–49.

[47] Noël L, Miegroet L V, Duysinx P. Analytical sensitivity analysis using the extended finite element method in shape optimization of bimaterial structures. *International Journal for Numerical Methods in Engineering*. 2016; **107**:669–695.

[48] Noël L, Duysinx P., Maute K. Damage process sensitivity analysis using an XFEM-Level Set framework. *In Proceedings of the 11th World Congress on Structural and Multidisciplinary Optimization* (WCSMO-11). 2015.

[49] Shi GH. Manifold method of material analysis. *in Transactions of the 9th Army Conference on Applied Mathematics and Computing*. Minneapolis, MN. 1991; 57–76.

[50] Shi GH. Simplex integration for manifold method, FEM, DDA and analytical analysis. *in Proceedings 1th international Forum on Discontinuous Deformation Analysis (DDA) and Simulations of Discontinuous Media*.TSI Press, Albuquerque, New Mexico, USA. 1996; 205–262.

[51] Lin JS. A mesh-based partition of unity method for discontinuity modelling. *Computer Methods in Applied Mechanics and Engineering*. 2003; **192**:1515–1532.

[52] Chen GQ, Ohnishi Y, Ito T. Development of higher-order manifold method. *International Journal for Numerical Methods in Engineering*. 1998; **43**:685–712.

[53] Lu M. High-order manifold method with simplex integration. *in Proceedings 5th International Conference on the Analysis of Discontinuous Deformation*. Wuhan, China. 2002; 75–83.

[54] Kourepinis D, Bicanic N, Pearce CJ. A higher-order variational numerical manifold method formulation and simplex integration strategy. *in Proceedings 6th International Conference on the Analysis of Discontinuous Deformation*. Trondheim, Norway. 2003; 145–152.

[55] Su HD, Xie XL, Liang QY, Automatic programming for high-order numerical manifold method, *in Proceedings 6th International Conference on the Analysis of Discontinuous Deformation*. Trondheim, Norway. 2003; 153–160.

[56] Babuska I, Melenk JM. Partition of unity method. *International Journal for Numerical Methods in Engineering*. 1997; **40**:727–758.

[57] An XM, Li LX, Ma GW, Zhang HH. Prediction of rank deficiency in partition of unity-based methods with plane triangular or quadrilateral meshes. *Computer Methods in Applied Mechanics and Engineering*. 2011; **200**(5–8):665–674.

[58] An XM, Liu XY, Zhao ZY, He L. Proof of linear independence of flat-top PU-based high-order approximation. *Engineering Analysis with Boundary Elements*. 2014; **44**:104–111.

[59] Ghasemzadeh H, Ramezanpour MA, Bodaghpour S. Dynamic high order numerical manifold method based on weighted residual method. *International Journal for Numerical Methods in Engineering*. 2014; **100**:596–619.

[60] Fan H, Zheng H, He SM. S-R decomposition based numerical manifold method. *Computer Methods in Applied Mechanics and Engineering*. 2016; **304**: 452–478.

[61] Ma GW, An XM, Zhang HH, Li LX. Modelling complex crack problems using the numerical manifold method. *International Journal of Fracture*. 2009; **156**:21–35.

[62] Wu ZJ, Wong LNY. Modeling cracking behavior of rock mass containing inclusions using the enriched numerical manifold method. *Engineering Geology*. 2013; **162**:1–13.

[63] Zhang HH, Zhang SQ. Extract of stress intensity factors on honeycomb elements by the numerical manifold method. *Finite Elements in Analysis and Design*. 2012; **59**:55–65.

[64] Zheng H, Xu DD. New strategies for some issues of numerical manifold method in simulation of crack propagation. *International Journal for Numerical Methods in Engineering*. 2014; **97**:986–1010.

[65] Chiou YJ, Lee YM, Tsay RJ. Mixed mode fracture propagation by manifold method. *International Journal of Fracture*. 2002; **114**:327–347.

[66] Zhang GX, Sugiura Y. Hasegawa H, Wang GL. The second order manifold method with six node triangle mesh. *Journal of Structural Mechanics and Earthquake Engineering*. 2002; **19**(1):1–9.

[67] Tsay RJ, Chiou YJ, Chuang WL. Crack growth prediction by manifold method. *Journal of Engineering Mechanics*. 1999; **125**:884–890.

[68] Yang SK, Ma GW, Ren XH, Ren F. Cover refinement of numerical manifold method for crack propagation simulation. *Engineering Analysis with Boundary Elements*. 2014; **43**:37–49.

[69] Zheng H, Liu F, Li CG. The MLS-based numerical manifold method with applications to crack analysis. Internat. *International Journal of Fracture*. 2014; **190**(1-2):147–166.

[70] Ma GW, An XM, He L. The numerical manifold method: a review. *International Journal of Computational Methods*. 2010; **7**(1):1–32.

[71] Zienkiewicz OC, Taylor RL, Zhu JZ. *The Finite Element Method: Its Basis and Fundamentals (Sixth edition)*. Oxford: Butterworth-Heinemann. 2005.

[72] Ewalds H, R. Wanhill R. *Fracture mechanics*. New York: Edward Arnold. 1989.

[73] Karihaloo BL. *Fracture mechanics and structural concrete*. England: Longman Scientific & Technical. 1973.

[74] Zhang HH, Li LX, An XM, et al. Numerical analysis of 2-D crack propagation problems using the numerical manifold method. *Engineering analysis with boundary elements,* 2010; **34**(1):41–50.

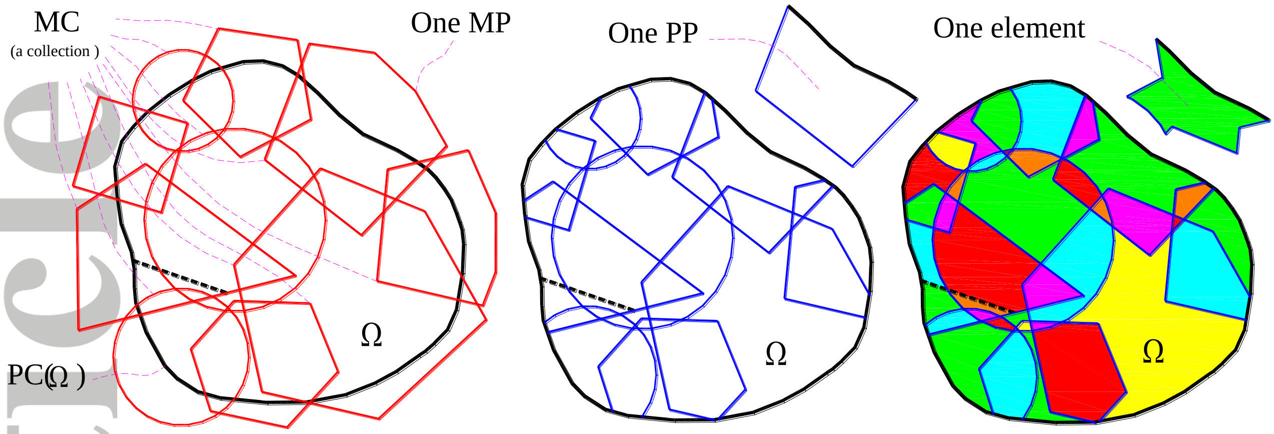

Figure1. PC, MC, MPs, PPs and MEs in NMM

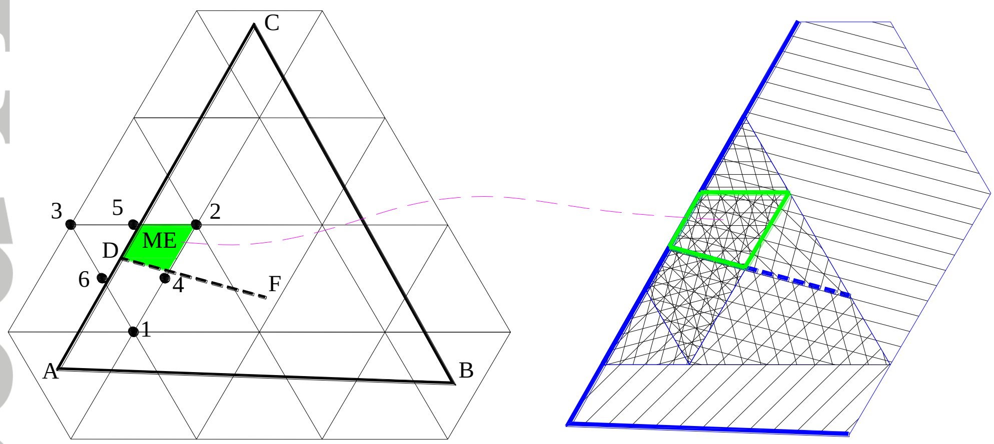

Figure 2. Problem domain under six-node triangular mesh

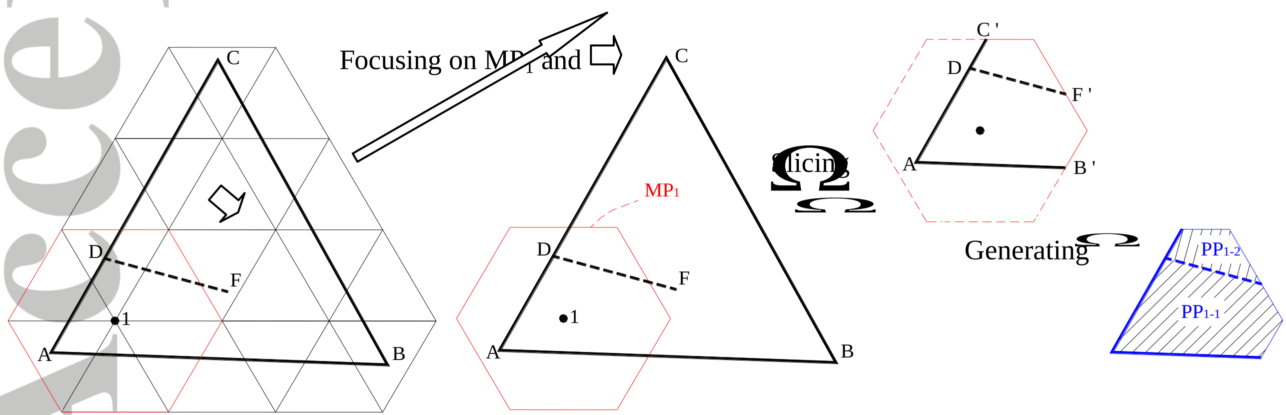

Figure 3. Formation process of physical patches $PP_{1\text{-}1}$ and $PP_{1\text{-}2}$

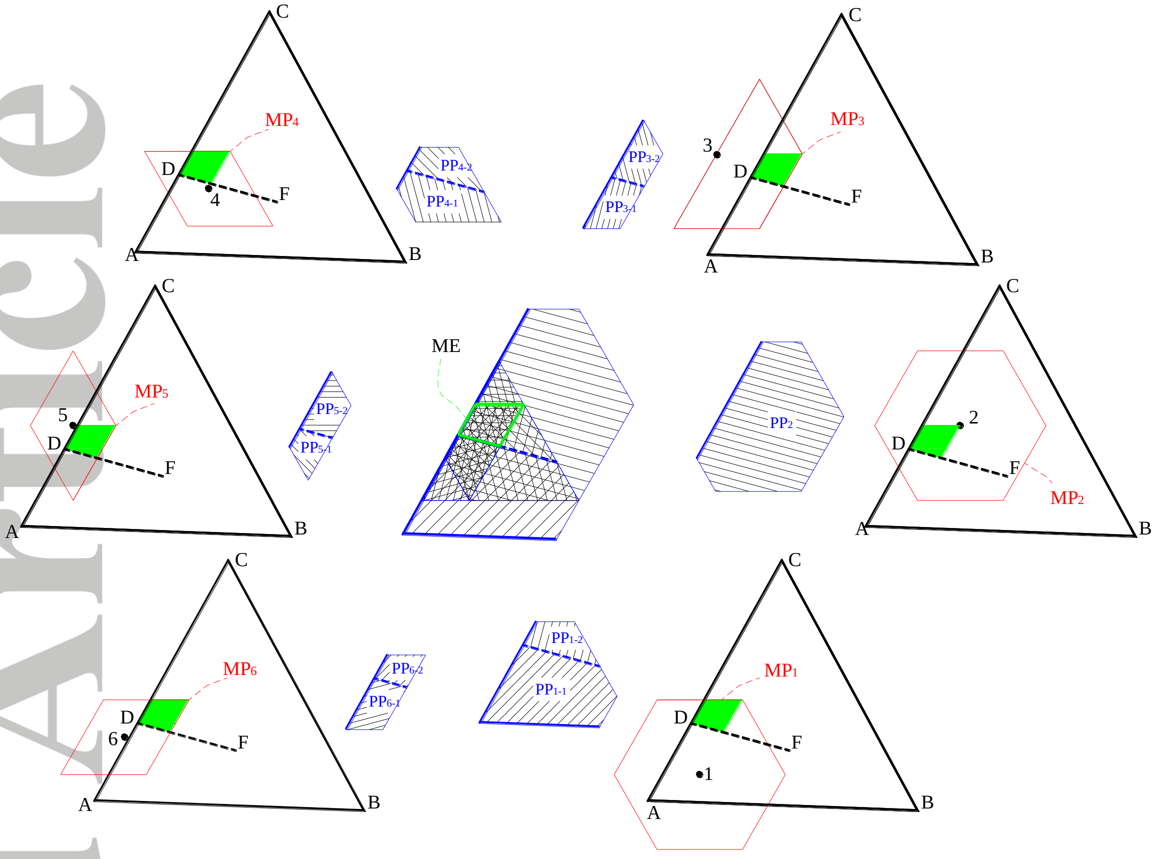

Figure 4. Formation process of ME

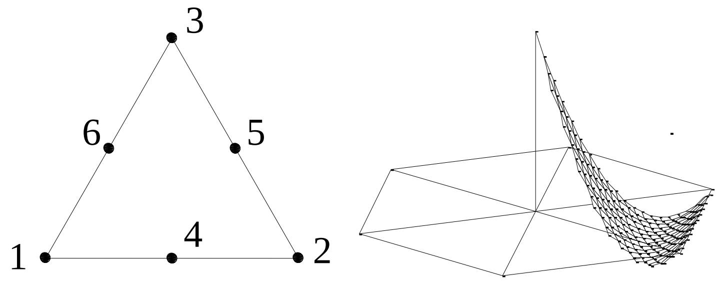

Figure 5. Partition of unity function of a six-node triangle

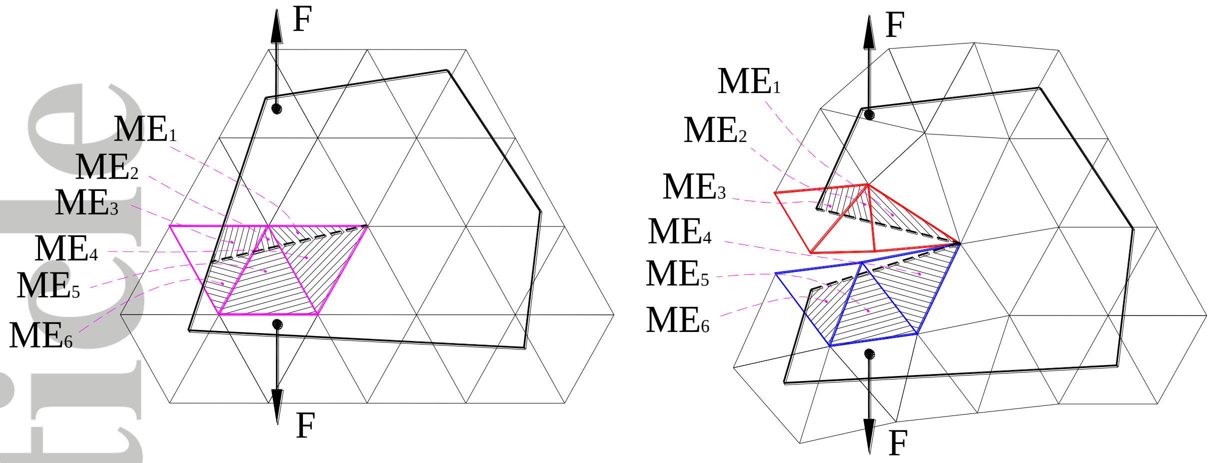

(a) Pre-deformation

(b) Post-deformation

Figure 6. Several MEs and MPs near the crack surfaces

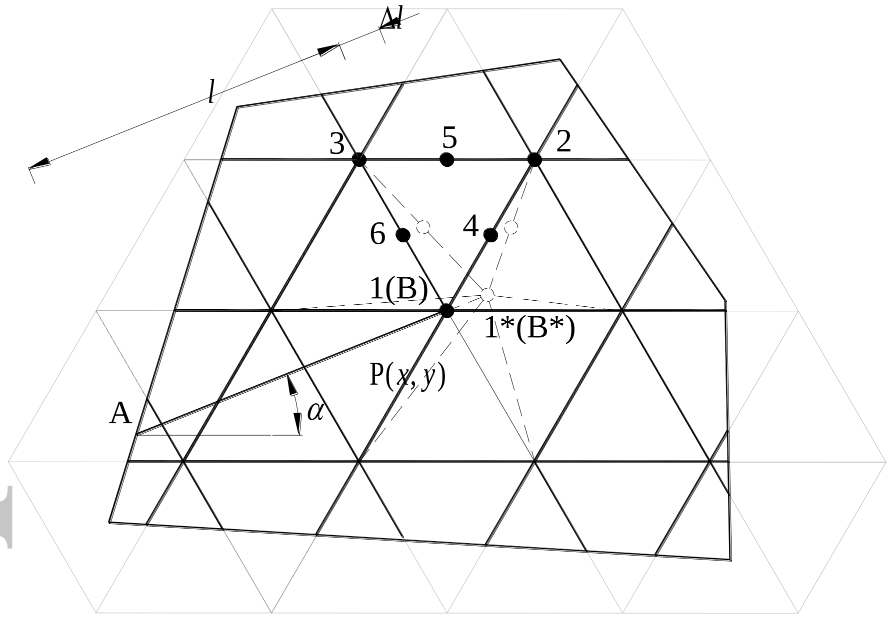

Figure 7. Simplest virtual crack extension method in which only crack-tip elements change their stiffness matrix

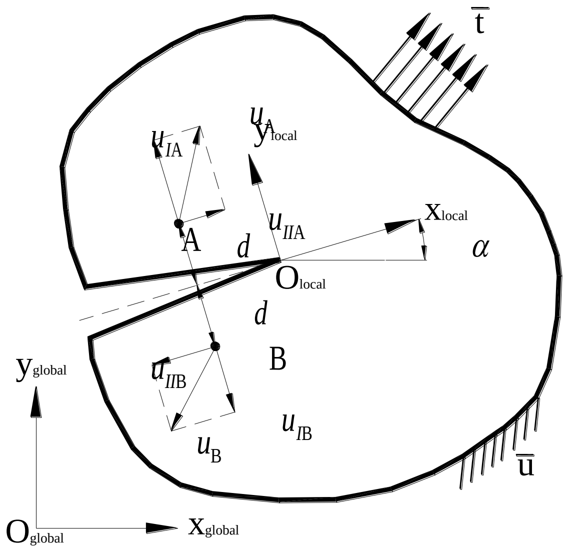

Figure 8. Decomposition of displacement field into mode-I and mode-II fields with respect to local crack-tip coordinate system

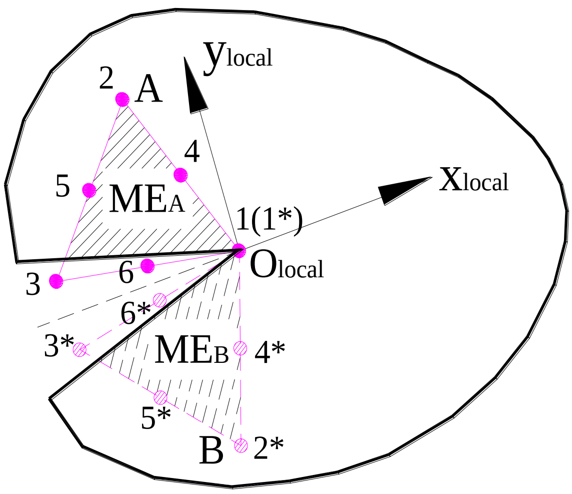

Figure 9. One crack-tip element and it's "stars"

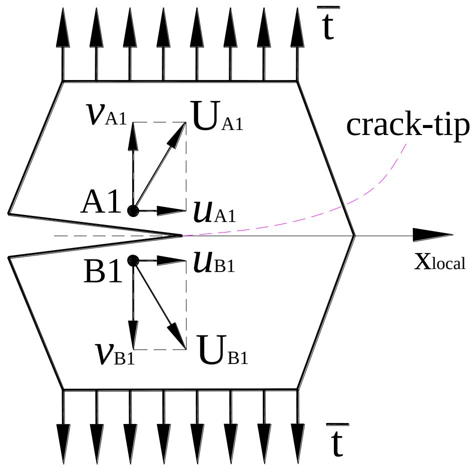

Figure 10. Points A1 and B1 and their displacements near the crack-tip

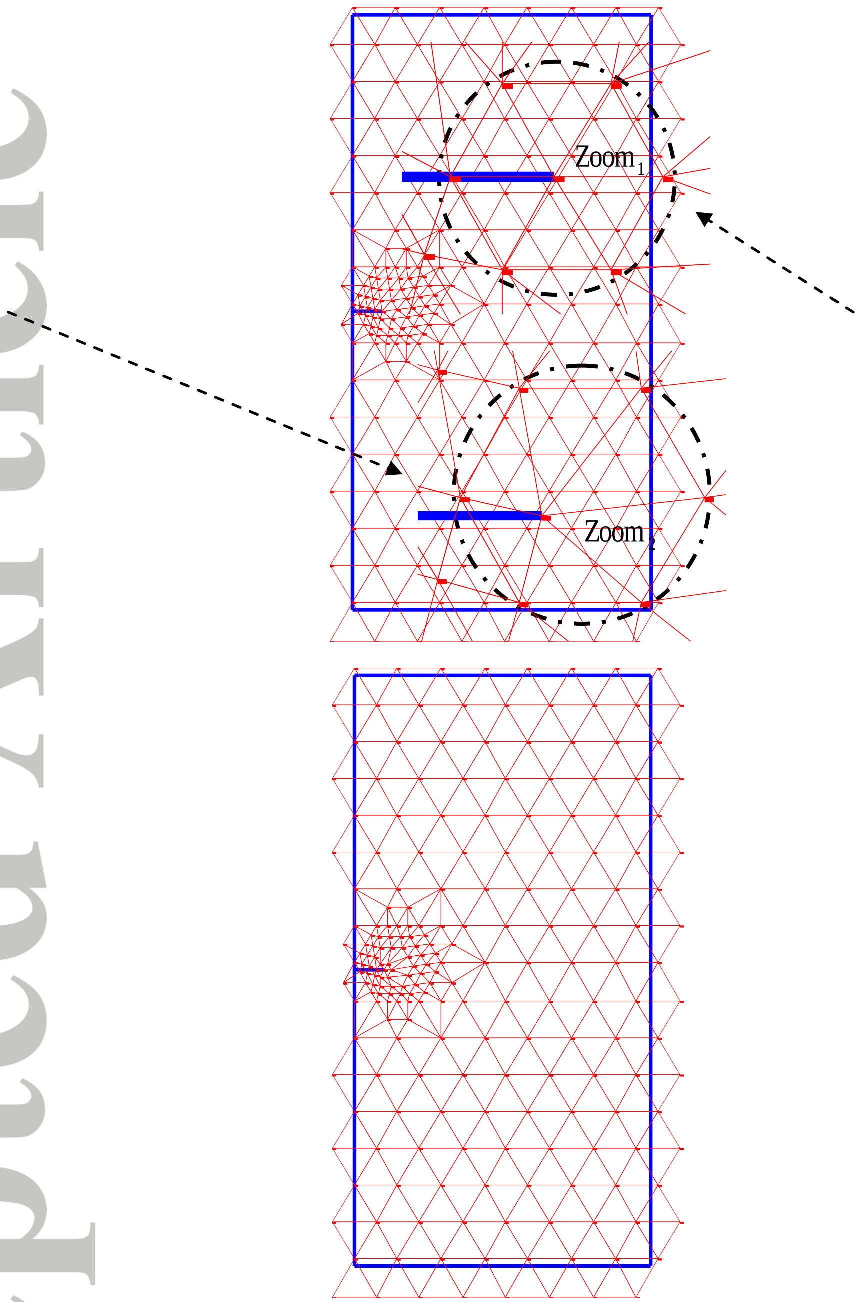

(a) (b)

Figure 12. (a) Asymmetrical configuration; (b) Symmetrical configuration (*a* = 0.1m)

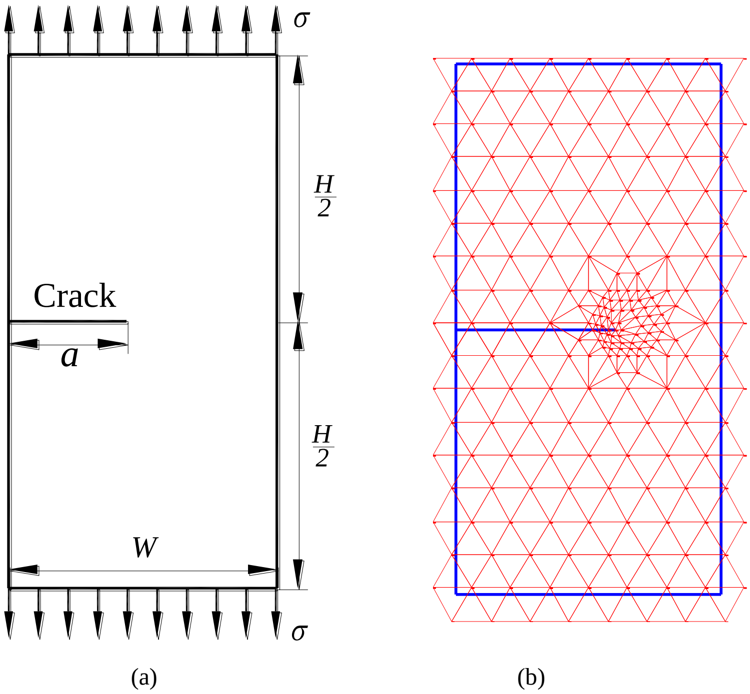

Figure 11. (a) Finite plate with an edge crack under tension; (b) Mathematical cover with LMCR near crack-tip (a = 0.6m)

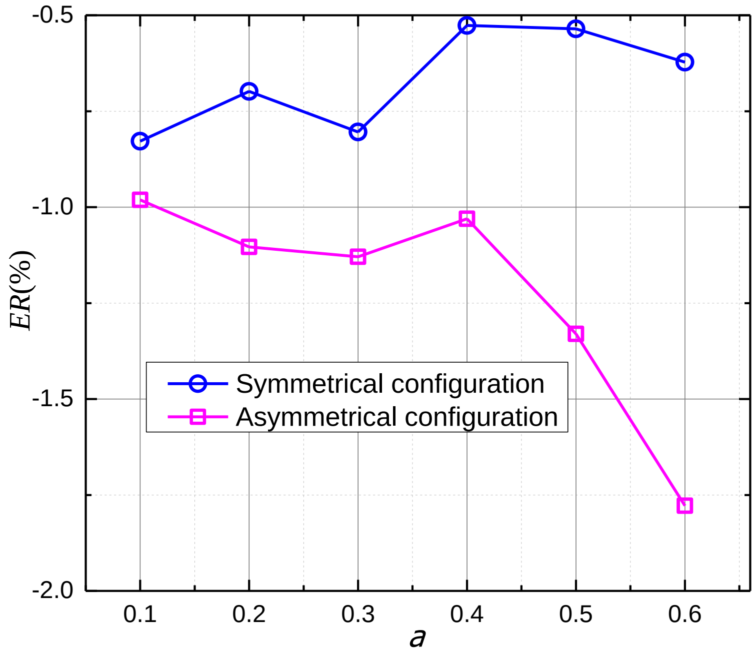

Figure 13. REs of K_I corresponding to the asymmetrical and symmetrical configurations

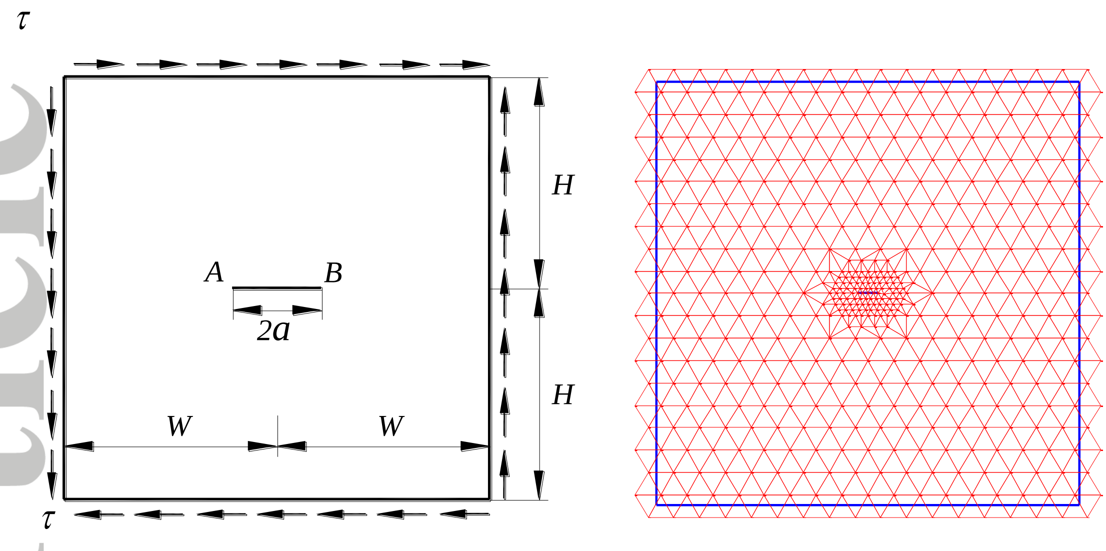

(a) (b)

Figure 14. (a) Plate with a central crack under shear; (b) Mathematical cover (20LNs) with LMCR near crack-tip

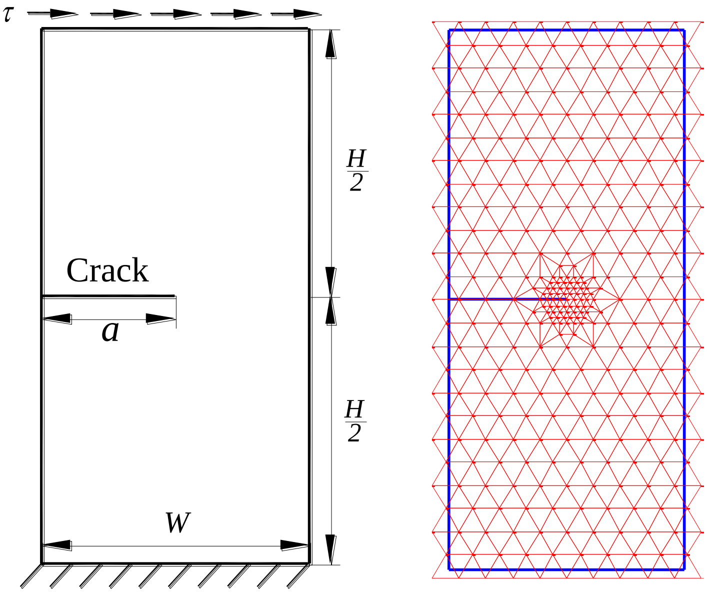

(a) (b)

Figure15. (a) Edge-cracked plate under mixed mode loading; (b) Mathematical cover (24LNs) with LMCR near crack-tip

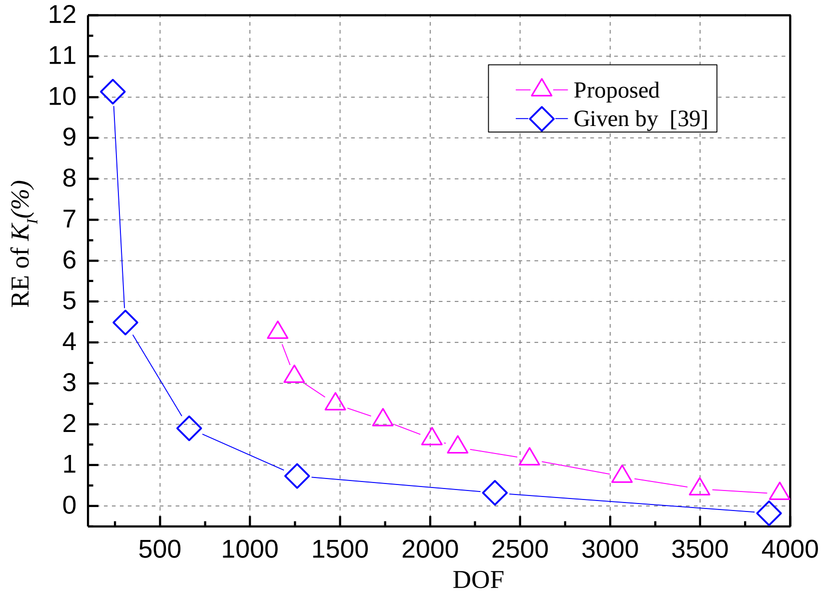

Figure16. Curve of relative error of K_I *vs.* DOF

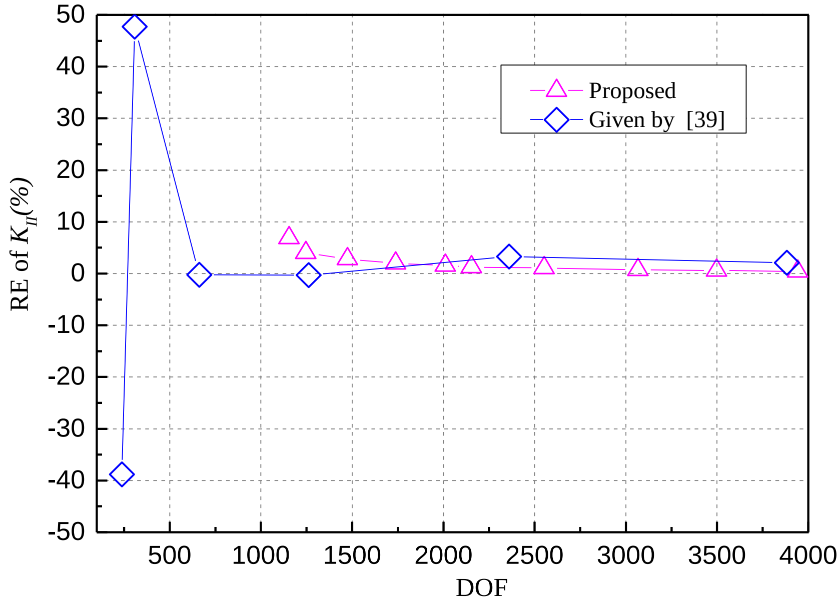

Figure17. Curve of relative error of K_{II} *vs.* DOF

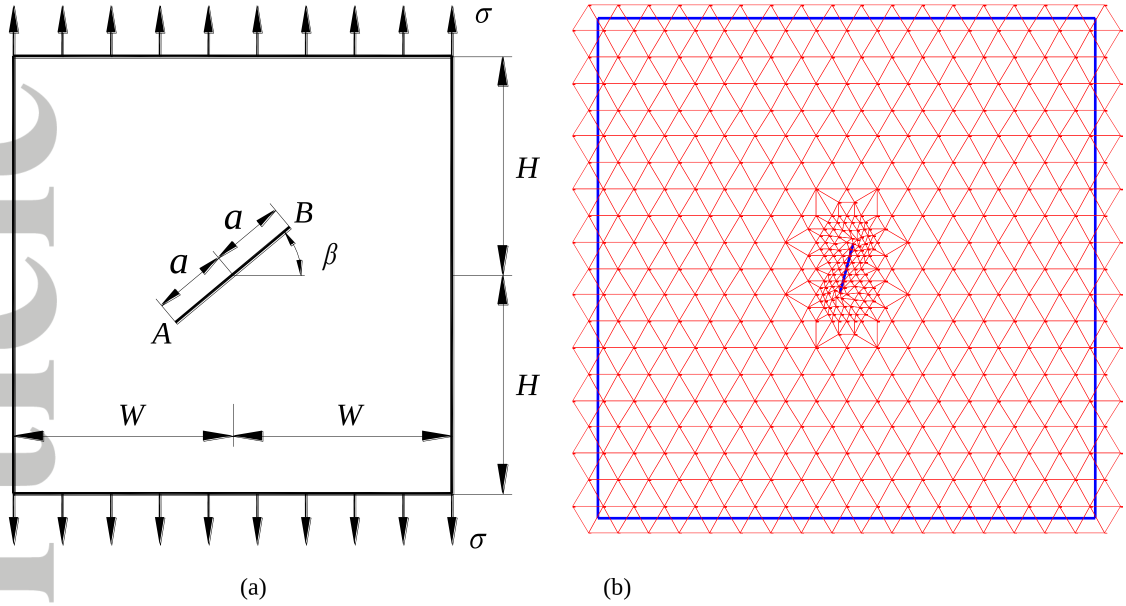

Figure18. (a) Square plate with an inclined center crack under tension; (b) Mathematical cover (20LNs) with LMCR (β=75°)

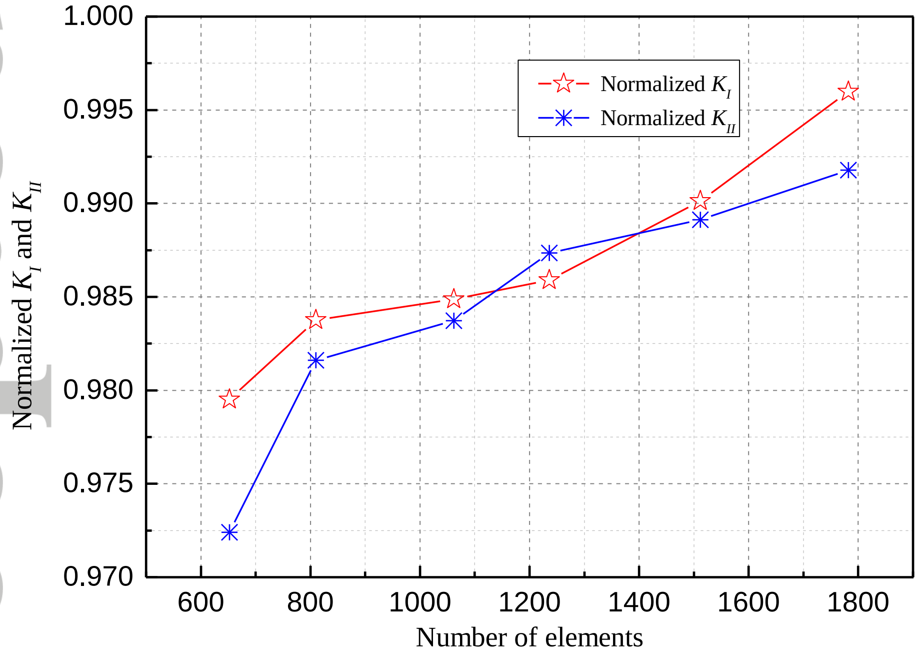

Figure19. Normalized K_I and K_{II} versus number of elements

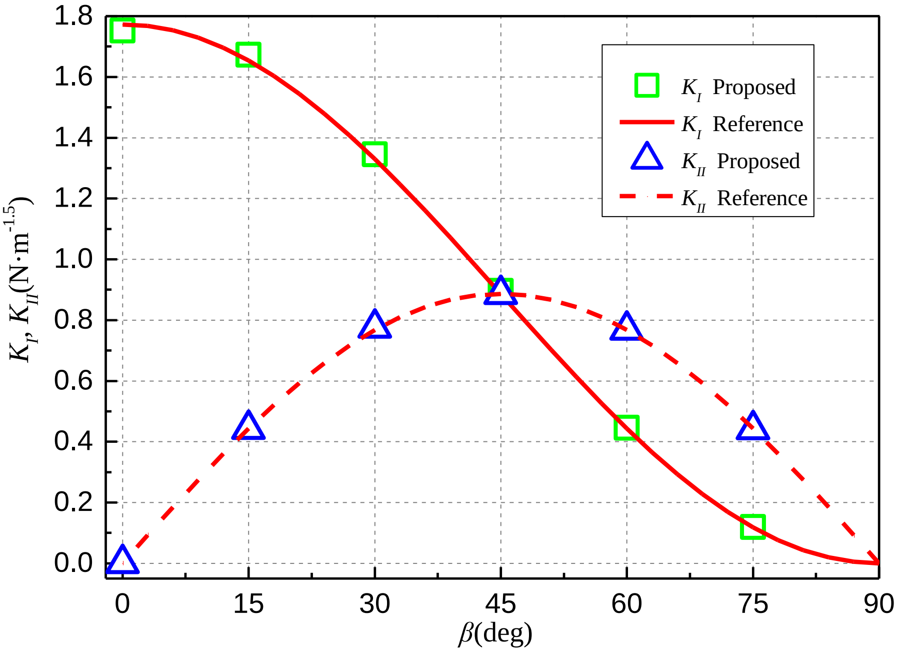

Figure 20. K_I and K_{II} versus inclined angle β

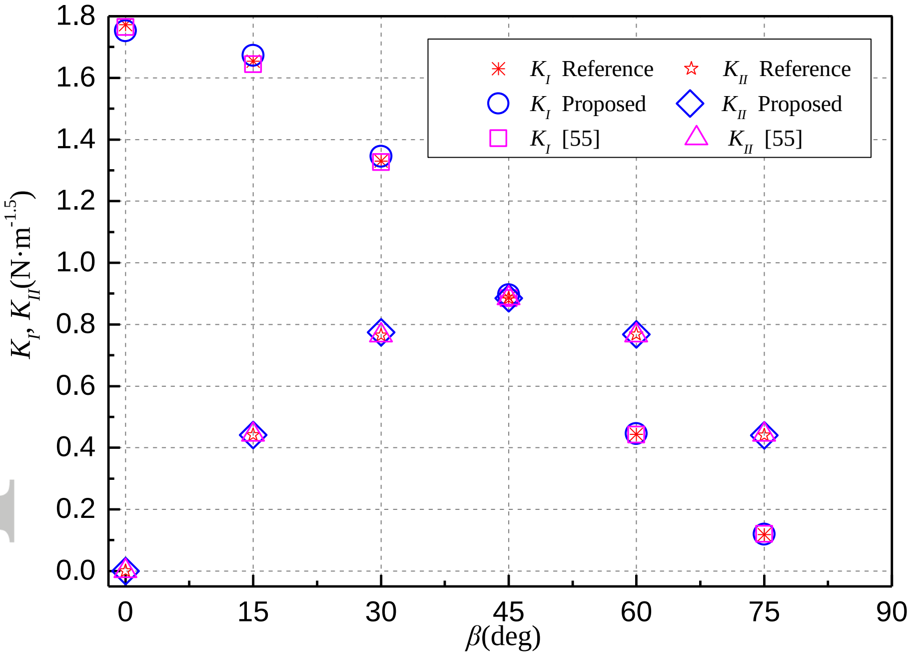

Figure 21. K_I and K_{II} versus inclined angle β

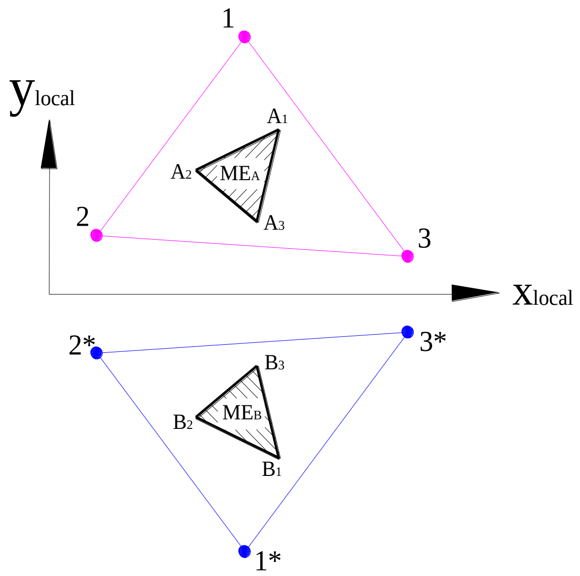

Figure A1. Two elements and the triangle meshes covering them

Table I K_I corresponding to different a (asymmetrical configuration)

a(m)	RV ($N \cdot m^{-1.5}$)	Finite difference approximation				Proposed analytic expression		
		Scale	CV	Normalized K_I	RE(%)	CV	Normalized K_I	RE(%)
0.1	0.663474	0.001	0.644396	0.9712	-2.8755	0.656965	0.9902	-0.9811
		0.0001	0.644718	0.9717	-2.8269			
		0.00001	0.644750	0.9718	-2.8221			
0.2	1.086478	0.001	1.054031	0.9701	-2.9864	1.074488	0.9890	-1.1036
		0.0001	1.054592	0.9707	-2.9348			
		0.00001	1.054648	0.9707	-2.9296			
0.3	1.611471	0.001	1.569055	0.9737	-2.6321	1.593274	0.9887	-1.1292
		0.0001	1.569918	0.9742	-2.5785			
		0.00001	1.570005	0.9743	-2.5732			
0.4	2.358024	0.001	2.303960	0.9771	-2.2928	2.333731	0.9897	-1.0302
		0.0001	2.305262	0.9776	-2.2376			
		0.00001	2.305392	0.9777	-2.2320			
0.5	3.542336	0.001	3.441687	0.9716	-2.8413	3.495218	0.9867	-1.3301
		0.0001	3.443683	0.9722	-2.7850			
		0.00001	3.443883	0.9722	-2.7793			
0.6	5.528026	0.001	5.372146	0.9718	-2.8198	5.429734	0.9822	-1.7781
		0.0001	5.375352	0.9724	-2.7618			
		0.00001	5.375673	0.9724	-2.7560			

Δl = Scale × the minimum value of side length of all elements; CV: calculation value; RV: reference value; RE: relative error = 100 × (CV-RV)/RV.

Table II K_I corresponding to different a (symmetrical configuration)

a(m)	RV ($N\cdot m^{-1.5}$)	Finite difference approximation				Proposed analytic expression		
		Scale	CV	Normalized K_I	RE(%)	CV	Normalized K_I	RE(%)
		0.001	0.649585	0.9791	-2.0935			
0.1	0.663474	0.0001	0.649837	0.9794	-2.0555	0.657980	0.9917	-0.8281
		0.00001	0.649862	0.9795	-2.0517			
		0.001	1.062999	0.9784	-2.1611			
0.2	1.086478	0.0001	1.063439	0.9788	-2.1205	1.078889	0.9930	-0.6985
		0.00001	1.063483	0.9788	-2.1165			
		0.001	1.582521	0.9820	-1.7965			
0.3	1.611471	0.0001	1.583199	0.9825	-1.7544	1.598515	0.9920	-0.8040
		0.00001	1.583267	0.9825	-1.7502			
		0.001	2.323594	0.9854	-1.4601			
0.4	2.358024	0.0001	2.324617	0.9858	-1.4167	2.345612	0.9947	-0.5264
		0.00001	2.324720	0.9859	-1.4124			
		0.001	3.470473	0.9797	-2.0287			
0.5	3.542336	0.0001	3.472043	0.9802	-1.9844	3.523378	0.9946	-0.5352
		0.00001	3.472200	0.9802	-1.9799			
		0.001	5.415535	0.9797	-2.0349			
0.6	5.528026	0.0001	5.418057	0.9801	-1.9893	5.493629	0.9938	-0.6222
		0.00001	5.418309	0.9802	-1.9847			

Δl = Scale × the minimum value of side length of all elements; CV: calculation value; RV: reference value; RE: relative error = 100 × (CV-RV)/RV.

Table III K_{II} corresponding to different LNs

LNs	CV	Normalized K_{II}	RE (%)	Position
16	3.930172	0.9916345	-0.8365	Crack-tip A
	3.930092	0.9916143	-0.8385	Crack-tip B
18	3.933724	0.9925306	-0.7469	Crack-tip A
	3.933670	0.9925172	-0.7483	Crack-tip B
20	3.948841	0.9963448	-0.3655	Crack-tip A
	3.948728	0.9963163	-0.3683	Crack-tip B

Reference value (RV): K_{II} = $3.963327 N\cdot mm^{-1.5}$; CV: calculation value; RE: relative error = 100 × (CV-RV)/RV.

Table IV K_I and K_{II} corresponding to different LNs

LNs/DOFs	CV	Normalized	RE (%)	SIFs
12/1154	32.557840	0.9576	-4.2416	K_I
	4.237557	0.9313	-6.8668	K_{II}
14/1246	32.923632	0.9683	-3.1657	K_I
	4.368358	0.9601	-3.9921	K_{II}
16/1474	33.153561	0.9752	-2.4895	K_I
	4.422125	0.9719	-2.8104	K_{II}
18/1738	33.285322	0.9790	-2.1019	K_I
	4.459334	0.9801	-1.9926	K_{II}
20/2010	33.443285	0.9836	-1.6373	K_I
	4.479038	0.9844	-1.5596	K_{II}
22/2154	33.510891	0.9856	-1.4385	K_I
	4.494161	0.9877	-1.2272	K_{II}
24/2552	33.611335	0.9886	-1.1431	K_I
	4.501426	0.9893	-1.0675	K_{II}
28/3066	33.755554	0.9928	-0.7189	K_I
	4.516238	0.9925	-0.7420	K_{II}
30/3498	33.860317	0.9958	-0.4108	K_I
	4.522871	0.9940	-0.5962	K_{II}
32/3942	33.897472	0.9969	-0.3015	K_I
	4.530942	0.9958	-0.4188	K_{II}

Reference value (RV): $K_I = 34.00\text{N}\cdot\text{m}^{-1.5}$, $K_{II} = 4.55\text{N}\cdot\text{m}^{-1.5}$; CV: calculation value;
RE: relative error = 100 × (CV-RV)/RV.

Table V K_I and K_{II} corresponding to the different elements ($\beta = 60°$)

Elements	LNs	K_I			K_{II}		
		CV	Normalized	RE(%)	CV	Normalized	RE(%)
652	16	0.434032	0.9795	-2.0494	0.746321	0.9724	-2.7588
810	18	0.435915	0.9838	-1.6246	0.753380	0.9816	-1.8391
1062	22	0.436415	0.9849	-1.5117	0.755002	0.9837	-1.6278
1236	24	0.436863	0.9859	-1.4106	0.757787	0.9874	-1.2649
1512	28	0.438738	0.9901	-0.9874	0.759152	0.9891	-1.0871
1782	30	0.441334	0.9960	-0.4017	0.761187	0.9918	-0.8219

Reference value (RV): $K_I = 0.443113\text{N}\cdot\text{m}^{-1.5}$, $K_{II} = 0.767495\text{N}\cdot\text{m}^{-1.5}$; CV: calculation value;
RE: relative error = 100 × (CV-RV)/RV.